WATER RESOURCES RESEARCH, VOL. 49, 1988–2012, doi:10.1002/wrcr.20180, 2013

# Long-term trends in evapotranspiration and runoff over the drainage basins of the Gulf of Mexico during 1901–2008

Mingliang Liu,[1,2] Hanqin Tian,[1] Qichun Yang,[1] Jia Yang,[1] Xia Song,[1]
Steven E. Lohrenz,[3] and Wei-Jun Cai[4]

Received 9 May 2012; revised 25 February 2013; accepted 2 March 2013; published 23 April 2013.

[1] The Gulf of Mexico (GOM) is facing large pressures from environmental changes since the beginning of the last century. However, the magnitude and long-term trend of total water discharge to the GOM and the underlying processes are not well understood. In this study, the dynamic land ecosystem model (DLEM) has been improved and applied to investigate spatial and temporal variations of evapotranspiration (ET) and runoff ($R$) over drainage basins of the GOM during 1901–2008. Modeled ET and discharge were evaluated against upscaled data sets and gauge observations. Simulated results demonstrated a significant decrease in ET at a rate of 15 mm $yr^{-1}$ $century^{-1}$ and an insignificant trend in runoff/precipitation ($R/P$) and river discharge over the whole region during 1901–2008. However, the trends in estimated water fluxes show substantial spatial and temporal heterogeneities across the study region. Generally, in the west arid area, ET, $R$, and $R/P$ decreased; while they increased in the eastern part of the study area during the last 108 years. In the recent 30 years, this region experienced a substantial decrease in $R$. Factorial simulation experiments indicate that climate change, particularly $P$, was the dominant factor controlling interannual variations of ET and $R$; while land use change had the same magnitude of effects on long-term trends in water fluxes as climate change did. To eliminate modeling uncertainties, high-resolution historical meteorological data sets and model parameterizations on anthropogenic effects, such as water use and dam constructions, should be developed.

**Citation:** Liu, M., H. Tian, Q. Yang, J. Yang, X. Song, S. E. Lohrenz, and W.-J. Cai (2013), Long-term trends in evapotranspiration and runoff over the drainage basins of the Gulf of Mexico during 1901–2008, *Water Resour. Res.*, *49*, 1988–2012, doi:10.1002/wrcr.20180.

## 1. Introduction

[2] The global water cycle has been substantially altered by the changing climate and intensifying human activities [*Hutjes et al*., 1998; *Jackson et al*., 2001; *Foley et al*., 2005; *Huntington*, 2006]. Increased air temperature ($T$) enlarges the holding capacity of air moisture and potentially increases the evapotranspiration (ET), which eventually intensifies precipitation ($P$) [*Intergovernmental Panel on Climate Change (IPCC)*, 2007]. Human behavior changes the water cycle through altering land cover (LC), withdrawing surface and ground water, changing rivers flow paths and the infiltration capacity [*DeFries and Eshleman*, 2004; *Huntington*, 2006]. The effects of human activities on water resources are spatially explicit, and there are still many arguments on how land use change affects runoff ($R$) processes. For example, deforestation could increase runoff by decreasing ET and the infiltration capacity [*Bosch and Hewlett*, 1982; *Andreassian*, 2004; *Farley et al*., 2005; *Bormann et al*., 2007]. However, other studies have suggested that deforestation caused by agricultural land expansion tends to consume more water because of huge irrigation water use compared with natural ecosystems [*Liu et al*., 2008].

[3] Attributing driving forces to the dynamics of the water cycle is another challenge. Paired watershed experiments and statistical methods are watershed-specific and thus are difficult to apply elsewhere [*Liu et al*., 2012]. In addition, understanding how human activities interact with climate in changing water fluxes is far from sufficient [*Vorosmarty and Sahagian*, 2000; *Jackson et al*., 2001; *Piao et al*., 2007]. Some scientists have emphasized the effects of climate and/or atmospheric chemical compositions [*Gedney et al*., 2006; *McLaughlin et al*., 2007; *Qian et al*., 2007], while others highlighted the importance of human influences in the water cycle [*Vorosmarty and Sahagian*, 2000; *Jackson et al*., 2005; *Sun et al*., 2005]. By using factorial experiments, it is possible to quantify the consequences of different combination of environmental and human-caused factors on water fluxes [*Shi et al*., 2011]. Several studies have attempted to reconstruct historical patterns of

[1]International Center for Climate and Global Change Research and School of Forestry and Wildlife Sciences, Auburn University, Auburn, Alabama, USA.
[2]Department of Civil and Environmental Engineering, Washington State University, Pullman, Washington, USA.
[3]The School for Marine Science and Technology, University of Massachusetts Dartmouth, New Bedford, Massachusetts, USA.
[4]School of Marine Science and Policy, University of Delaware, Newark, DE 19716, USA.

Corresponding authors: M. Liu, Department of Civil and Environmental Engineering, Washington State University, Pullman, WA 99164, USA (mingliang.liu@wsu.edu); H. Tian, School of Forestry and Wildlife Sciences, Auburn University, Auburn, AL 36849, USA (tianhan@auburn.edu).


0043-1397/13/10.1002/wrcr.20180

river discharge and to identify their driving forces through combining long-term observations with hydrological models [*Gedney et al*., 2006; *Piao et al*., 2007; *Dai et al*., 2009]. These global scale studies, however, are too coarse to represent watershed-scale interactions between climate change and land use. Hence, the combination of field observations, remotely sensed data, and process models is becoming an efficient way to study water fluxes at regional scales [*Dirmeyer et al*., 1999; *Guo et al*., 2006; *Fisher et al*., 2008; *Jung et al*., 2009, 2010; *Sun et al*., 2011; *Vinukollu et al*., 2011a, 2011b]. These intermediate-scale modeling efforts can enhance our understanding of climate change and human activities affect the vertical and horizontal water fluxes at regional scales.

[4] The Gulf of Mexico (GOM) is one of the largest semienclosed marine systems of the world, which is sensitive and vulnerable to the environmental changes over the drainage area [*MacCracken et al*., 2009]. It contains the second largest zone of coastal hypoxia in the world. It is located on the northern GOM continental shelf adjacent to the outlets of the Mississippi and Atchafalaya rivers [*Rabalais et al*., 2002b]. The drainage area of the GOM has experienced significant land use changes over the last century. The industrialization of agriculture since the 1950s has caused a dramatic change in the agricultural LC and land use practices in the Mississippi River basin [*Foley et al*., 2004]. For example, soybean cultivation has expanded by about 200% by replacing maize, wheat, and pastures in the Upper Mississippi River [*Schilling et al*., 2010]. Land use change may alter the magnitude and seasonal variations of fresh water and nutrients discharge to the coastal area, which affect the productivity and biogeochemical cycles of the marine ecosystem [*Turner and Rabalais*, 2003; *Donner et al*., 2004; *Schilling et al*., 2010]. Currently, our understandings are still insufficient on how human activities interact with climate factors in changing water resources in the drainage basins of the GOM. The objective of this study is to investigate how climate change and human activities may have affected the freshwater discharge to the GOM by improving and applying a process-based land ecosystem model—the dynamic land ecosystem model (DLEM). This article consists of five parts: (1) descriptions of the model and major improvements; (2) model evaluations; (3) simulation results on ET and *R* during 1901–2008; (4) attribution of the temporal and spatial patterns of water fluxes to changes in major climate variables (*T* and *P*) and land use; and (5) discussion.

## 2. Study Area

[5] The drainage basins of the GOM cover an area of 5.37 million $km^2$ or 27% of continental North America (Figure 1). Increasing populations and intensifying land use activities in this area have caused serious long-term impacts on the natural ecosystems and coastal regions during the last century [*Environmental Protection Agency, Office of Water Gulf of Mexico Program*, 1994; *Donner et al*., 2002; *Rabalais et al*., 2002a]. For regional comparisons, the GOM drainage basin is divided into five major regions: East Coast of the GOM (EC), Mississippi-Atchafalaya River Basin (MARB), Texas Basin (TB), Rio Grande Basin (RGB), and Western and Southern Coast of the GOM (WSC) (Figure 1). Among these five regions, the MARB is the largest basin which covers more than 16% of the continental North America and supports about 70 million people (22% of U.S. population). The MARB is further divided into eight subbasins for regional analysis: Upper Missouri (UMO); Lower Missouri (LMO); Upper Mississippi (UMS); Lower Mississippi (LMS); Upper Ohio (UOH); Lower Ohio (LOH); Arkansas (AR); and Red and Ouachita (RO) (Figure 1).

## 3. Model and Improvements

[6] DLEM is a process-based land ecosystem model that couples major biogeochemical cycles, water cycle, and vegetation dynamics to make daily and spatially explicit estimates of fluxes of water, greenhouse gases (GHGs) (including $CO_2$, $CH_4$, and $N_2O$), and a variety of storage pools of carbon, nitrogen, and water in terrestrial ecosystems [*Chen et al*., 2006; *Ren et al*., 2007b; *Zhang et al*., 2007a; *Liu et al*., 2008, 2012; *Tian et al*., 2010c, 2011a; *Xu et al*., 2010]. It includes five core components: (1) biophysics, (2) plant physiology, (3) soil biogeochemistry, (4) dynamic vegetation, and (5) disturbance, land use, and management [*Tian et al*., 2010a]. Briefly, the biophysics component simulates instantaneous fluxes of energy, water, and momentum within land ecosystems and their exchanges with the surrounding environment. The plant physiology component simulates major physiological processes, such as plant phenology, carbon (C), and nitrogen (N) assimilation, respiration, allocation, and turnover. The soil biogeochemistry component simulates the dynamics of nutrient compositions and major microbial processes, including nutrient mineralization/immobilization, nitrification/denitrification, decomposition, and methane production/oxidation. The dynamic vegetation component simulates the structural dynamics of vegetation caused by natural and human disturbances. Like most dynamic global vegetation models, DLEM employs the concept of plant functional types (PFTs) to characterize terrestrial biomes. The disturbances, land use, and management component simulate cropland conversions, reforestation after cropland abandonment, and forest management practices such as harvest, thinning, fertilization, and prescribed fires.

[7] Recent improvements on the model include a redesign of grid structure, additional soil layers, revision of rainfall-runoff process, and an implementation of a river routing system. Hereafter, DLEM v1.0 refers to the old version of the model and DLEM v2.0 refers to the current version. Without special notification, DLEM refers to DLEM v2.0 throughout the paper.

### 3.1. Configuration for Subgrid Hierarchy

[8] As a distributed and spatially explicit ecosystem model, DLEM uses a regular grid as its fundamental simulation unit. In DLEM v1.0, each grid cell only has one PFT. In the current version, a cohort structure is used to represent multiple PFTs and LCs in each grid. Seven types of LC and water bodies can be specified in each grid, including vegetation cover, impervious surface, lake, stream, sea, bare ground, and glacier. The vegetation cover may contain at most five PFTs, among which four types are reserved for natural PFTs and one for crops. All LCs in each grid share a common soil water column, while each PFT is simulated independently in physiological and soil biogeochemical

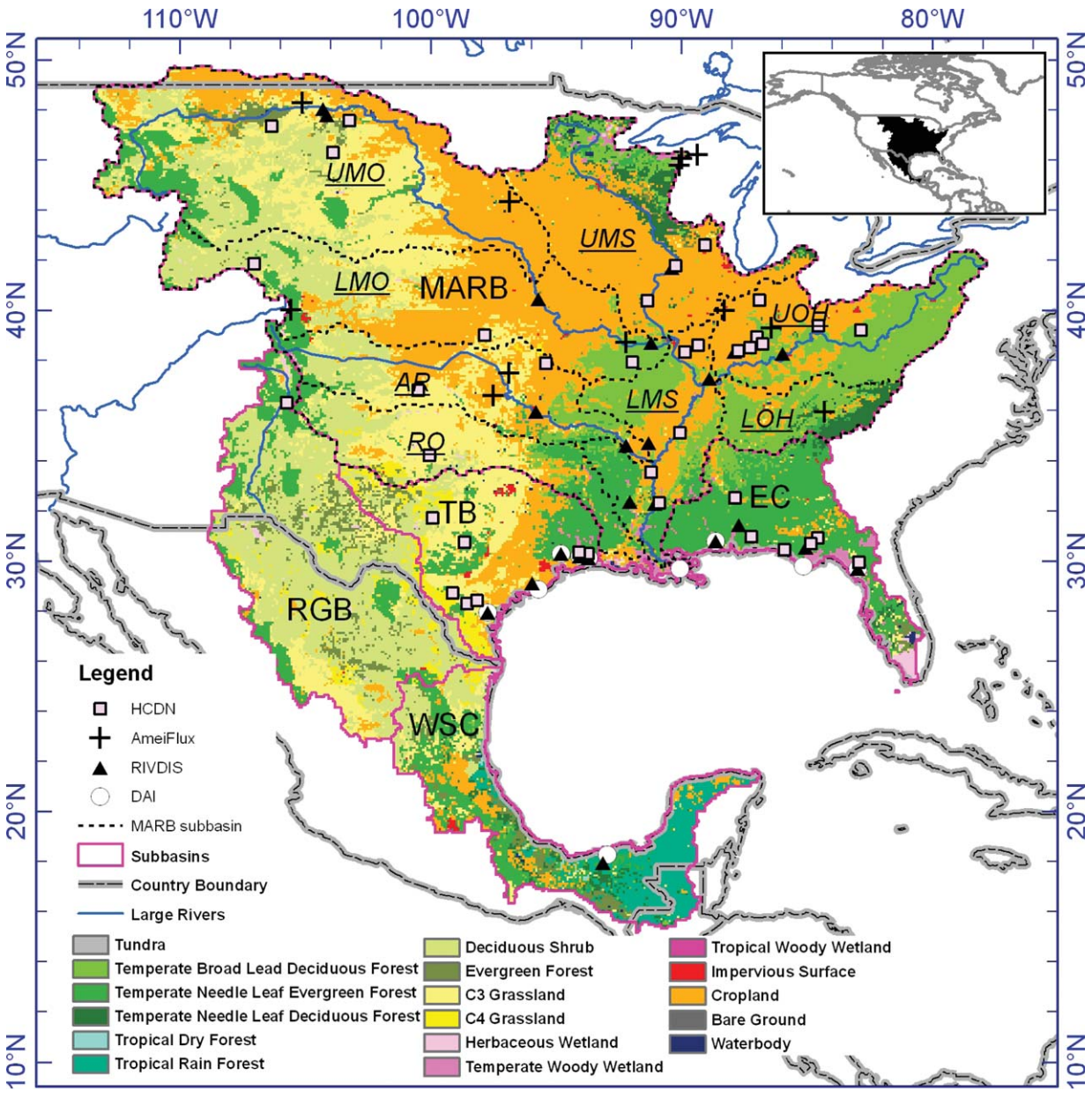


**Figure 1.** Study area, LC, and distributions of validation sites (LC shows the dominant type in each 5 arc min grid). The abbreviations of basin names: EC, East Coast of the GOM; MARB: Mississippi-Atchafalaya River Basin; UMO: Upper Missouri; LMO: Lower Missouri; UMS: Upper Mississippi; LMS: Lower Mississippi; UOH: Upper Ohio; LOH: Lower Ohio; AR: Arkansas; RO: Red and Ouachita; TB: Texas Basin; RGB: Rio Grande Basin; and WSC: Western and Southern Coast of the GOM.

processes. The interception of rainfall and snowfall by each PFT is also estimated individually. Detailed descriptions of the C and N pools and the major biogeochemical processes can be found in previous publications [*Ren et al*., 2007b; *Tian et al*., 2010a, 2010c, 2011a; *Xu et al*., 2010; *Liu et al*., 2012].

[9] DLEM v1.0 designated two layers of mineral soil with a depth of 0.5 and 1.0 m, respectively [*Liu et al*., 2008]. To enhance the model's ability to address water pressure for each PFT that has specific root distributions, the soil column is divided into 10 layers similar to the Community Land Model (CLM) [*Oleson et al*., 2004]. To account for the surface water storage, a pond above the soil water column was included in DLEM v2.0. Using the Simple Groundwater Model (SIMGM) as in CLM [*Niu et al*., 2007; *Oleson et al*., 2008], DLEM quantifies the water interactions between root zones and defines a virtual unconfined aquifer. Two ground water pools in the soil water column were considered: the water stored in an unconfined aquifer ($W_a$) and the total ground water ($W_t$) that included the water in the soil column and the water in the aquifer. Other water pools in each grid included lake ($W_{\text{lake}}$), stream ($W_{\text{stream}}$), sea ($W_{\text{sea}}$), surface runoff pool ($W_s$), subsurface drainage pool ($W_d$), snowpack ($W_{\text{snow}}$), and water interceptions by each PFT.

### 3.2. Parameterizations on Major Hydrological Processes

[10] Some parameterization processes were kept the same in DLEM v2.0, including the partition of precipitation into snow and rainfall interception, canopy interception, snow sublimation, and snowmelt. The model descriptions on the aforementioned processes can be found in the supplement material of *Liu et al*. [2012]. New model improvements are summarized in the following sections.

#### 3.2.1. Rainfall Disaggregation

[11] In DLEM v1.0, as well as most of terrestrial ecosystem models, rainfall was assumed to be evenly distributed within a day. Without exceptions, this assumption may cause an underestimation on the Horton overland flow (i.e., rainfall exceeds the infiltration capacity). At the same time, it also affects the estimated timing of Dunne (saturated) overland flow. To avoid these problems, a disaggregation algorithm in DLEM v2.0 was introduced for the rainfall-runoff process while keeping biogeochemical and ecological processes running at a daily time step. In the model, $P$ is first divided into fractions of rainfall and snowfall according to $T$. Interceptions of rainfall and snowfall by each PFT is quantified by its leaf properties and leaf area index (LAI). Then the canopy throughfall is disaggregated into 2 h timepieces according to the method of *Connolly et al*. [1998]. No disaggregation treatment is applied to snowfall. The intercepted snowfall will fall on the ground to form snowpack.

#### 3.2.2. Surface Runoff and Baseflow

[12] In DLEM v1.0, surface runoff is generated when the first soil layer (i.e., the upper layer with the depth of 50 cm) becomes saturated [*Liu et al*., 2008, 2012]. To consider the effects of local topography on surface runoff and water table, DLEM is combined with the SIMTOP model [*Niu et al*., 2005], which is based on the TOPMODEL runoff scheme of *Chen and Kumar* 2001. The detail equations and processes can be found in Appendix A.

#### 3.2.3. Soil Moisture Movement and ET Process

[13] For the soil moisture movement, DLEM follows the CLM with Richards equation [*Oleson et al*., 2008]. The transpiration loss from each soil layer is the area-weighted sum of all PFTs. The transpiration is calculated by the Penman-Monteith approach [*Wigmosta et al*., 1994]. To consider the $CO_2$ fertilization effects on stomatal conductance, a response curve was added according to field observations. Appendix B lists major equations and improvements on the evapotranspiration processes.

#### 3.2.4. River Routing Process

[14] To route the runoff from each grid cell to the stream network, HYDRA model has been combined into DLEM [*Coe*, 2000]. The simulating time step for the water flow from the land to the water pools is 30 min. The daily surface $R$ and baseflow are evenly allocated into each 30 min slot, and thereafter they directly flow into the surface water pool ($W_s$) and subsurface drainage pool ($W_d$), respectively. Then, the water in these water pools discharges into the downstream grid with a flow rate determined by their residence time [*Coe*, 2000]. Appendix C describes major equations and processes.

## 4. Data and Simulation

### 4.1. Geographic Background and Land Use Data Sets

[15] To drive DLEM v2.0, time-series spatial data sets with a spatial resolution of 5 × 5 arc min (~9.2 × 9.2 km at the equator) are developed. There are three major groups of input data to DLEM v2.0: the environmental variables that do not change over time, such as the soil properties, elevation, and the river network; the physiological and biogeochemical parameters of each PFT; and the driving factors including climate and atmospheric chemistry (e.g., N deposition and atmospheric $CO_2$), human disturbances such as land use conversion, and management practices.

[16] These data sets were developed from multiple sources. Table 1 lists the major data sources and their resolutions. For soil properties for different layers, the top five soil layers (i.e., from ground surface to one meter depth with 20 cm interval for each layer), or the value of the top soil layer if the remaining layers have no data, are used for all 10 soil layers in DLEM. In the river flow direction map, those island grids without flow direction are identified and assigned with directions so that all exotic river discharges can finally flow to the ocean.

[17] The land use and LC in DLEM v2.0 are processed as fractions of each PFT and nonvegetated cover. To generate these historical annual data sets from 1901 to 2008, the following steps are involved. The first step is to identify the constant fractional cover of the land and the water within each grid. It is assumed that surface areas of lakes, streams, oceans, glaciers, and bare ground in each grid do not change over time. The lake and stream surface areas are estimated from the Shuttle Radar Topography Mission (SRTM) Water Body Data (SWBD) products (Table 1). The fractional distributions of the glaciers and bare ground are quantified with the GLC2000. The second step is to calculate percentages of each natural PFT within each grid. The distributions of contemporary PFTs are integrated from multiple data sources: the GLC2000, global potential vegetation map, and the Global Lakes and Wetlands Database (GLWD) (Table 1). The methodologies for the map integration are based on *Liu and Tian* [2010] and *Tian et al*. [2010a]. The final step is to generate historical distributions of impervious surface and cropland at annual time step. By comparing remote sensing-based global impervious surface data with HYDE urban area data (Table 1), the average fraction of impervious surface in urban area is calculated. Then this fraction is used to convert urban area to impervious surface area for historical periods. With the annual fractional impervious surface area and the nonvegetated covers (i.e., lakes, streams, glaciers, bare ground, and oceans), the total fractional vegetated area is identified. Finally, historical fractional cropland data are generated by integrating HYDE2005 cropland area data with the fractional vegetated area. Limited by data availability, no land use/LC change is assumed after 2005.

[18] For agricultural ecosystems, a cropping system map is produced by combining the crop harvest area and the global crop area distributions from *Monfreda et al*. [2008]. In DLEM, the cropland is treated as either irrigated or non-irrigated. Therefore, the fractional data of total area available for irrigation (TAAI) (Table 1) was converted into a Boolean map with a criterion of 30% irrigation rate in each

**Table 1.** Major Data Sources for Running DLEM

| Name | | Original Spatial Resolution | Data Source |
|---|---|---|---|
| Environmental variables | DEM | 30 arc sec | HYDRO1K, EROS Data Center, U.S. Geological Survey |
| | River network | 5 arc min | *Graham et al*. 1999 |
| | Soil properties (%silt, % sand, %clay, pH) | 0.5° | ISRIC-WISE [*Batjes*, 2006] |
| | Land area | 30 arc sec | GLC2000 [*Latifovic et al*., 2004] |
| | Lake and stream surface area | 1 arc sec | Shuttle Radar Topography Mission (SRTM) Water Body Data (SWBD) products, http://www2.jpl.nasa.gov/srtm/ |
| Driving forces | Potential vegetation map | 5 arc min | *Ramankutty and Foley* 1999 |
| | Wetland distribution | 30 arc sec | Global Lakes and Wetlands Database (GLWD) [*Lehner and Doll*, 2004] |
| | Historical cropland and urban area | 5 arc min (1700–2005) | History Database of the Global Environment (HYDE), ftp://ftp.mnp.nl/hyde/hyde_sept08 [*Goldewijk and Ramankutty*, 2004] |
| | Impervious surface area | 1 km | [*Elvidge et al*., 2007] |
| | Crop area and crop types | 5 arc min | *Monfreda et al*. 2008; U.S. Census of Agriculture, http://www.agcensus.usda.gov |
| | Irrigation area | 5 arc min | International Water Management Institute (IWMI)'s Total Area Available for Irrigation (TAAI) data set [*Thenkabail et al*., 2009] |
| | Nitrogen fertilizer use | State level (1960–2008) | USDA Economic Research Service (http://www.ers.usda.gov/Data/FertilizerUse/) for U.S. and FAO global nitrogen fertilizer data for Mexico and Canada [*Food and Agriculture Organization of the United Nations*, 2006] |
| | Historical climate data | 0.5° (1901–2002) | CRU TS 2.1 [*Mitchell and Jones*, 2005] |
| | Contemporary climate data | 32 km (1979–2008) | NARR data set [*Mesinger et al*., 2006] |

grid, i.e., if the irrigated area is more than 30%, the grid is defined as irrigated; otherwise it is defined as nonirrigated. This percentage (30%) assures total irrigation area over North America is consistent with the original TAAI data. The historical nitrogen fertilizer use for major crops since 1960 is derived from United States Department of Agriculture (USDA) for the U.S. and Food and Agriculture Organization (FAO) global nitrogen fertilizer data for Mexico and Canada. For the period of 1900–1960, a linear increasing trend in nitrogen fertilizer use is assumed.

### 4.2. Reconstruction of Historical Meteorological Data

[19] The historical daily climate data were generated from high-resolution gridded met data products TS 2.1 from station observations by the Climatic Research Unit (CRU) of the University of East Anglia TS 2.1 and North America Regional Reanalysis (NARR) data set from a combination of modeled and observed data [*Mitchell and Jones*, 2005; *Mesinger et al*., 2006]. NARR data covered the period of 1979–2008 and had 32 km resolution. At first, NARR data were interpolated into 5 arc min resolution data with an inverse distance squared weighted interpolation method. Then, for the period of 1901–1978, a revised delta method was used to combine monthly CRU data with daily NARR data. The daily pattern of reconstructed historical climate data was from NARR, but the monthly mean $T$ and $P$ was perturbed with CRU data. The final climate data contained historical monthly anomalies in $P$ and $T$ (including monthly mean daily $T$, monthly mean minimum $T$, and monthly mean maximum $T$) from CRU and daily and spatial patterns from NARR. We assumed no long-term trends occurred in relative humidity and solar radiation. For the period of 1979–2008, the interpolated NARR reanalysis data sets were directly used. A brief description of the data process can be found in Appendix D.

[20] Comparisons of $T$ and $P$ were made between reconstructed historical met data and CRU data over the study area (Figure 2). The reconstructed historical $T$ and $P$ retained the interannual and decadal variations recorded in the CRU data set so they are valid for conducting long-term trend analyses. However, discrepancies between the CRU and NARR in spatial resolution and magnitude may introduce some uncertainties in this study. Another shortcoming of this method is that $P$ in the selected NARR year could not have been enough to reproduce historical decreases according to CRU data. To eliminate biases that might be derived from discontinuity of climate data sources, analyses over three time periods, i.e., 1901–1978, 1979–2008, and 1901–2008 were separated throughout this paper. Variation of trends in these different time periods could provide further information on the evolution of water flux variations over the study area.

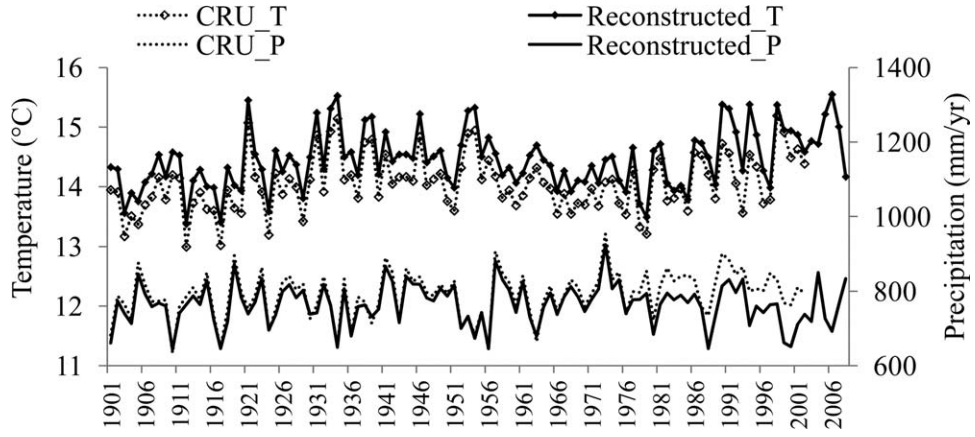


**Figure 2.** Reconstructed interannual variations of mean annual temperature and annual precipitation versus CRU climate data over the study area.

### 4.3. Simulation Experiments

[21] DLEM simulations included three runs: equilibrium, spinning-up, and transient runs. In the equilibrium run, the environmental conditions in the year 1900 (the climate was the average between 1901 and 1930; other environmental factors, including land use, atmospheric $CO_2$ concentration, and nitrogen deposition were static for the year 1900) are used to drive the model for achieving an equilibrium state that is defined as the interannual variation of net fluxes less than 0.1 g C $m^{-2}$ $yr^{-1}$ for carbon, 0.1 g N $m^{-2}$ $yr^{-1}$ for nitrogen, and 0.1 mm $m^{-2}$ $yr^{-1}$ for water within a 50 year simulation cycle. Three spin-up runs by using climate over the period of 1901–1930 were conducted to reduce the biases in the simulations toward the transient run [*Thornton and Rosenbloom*, 2005]. To quantify relative contributions of major environmental factors to variations in water fluxes, five transient simulation experiments for the period of 1901–2008 were set up as listed in Table 1. In the "Base" experiment, all environmental factors were transient, while in factor-controlled simulation experiments, only one or one group of environmental factors were transient and other factors are constant. In the "FixT" and "FixP" experiments, all transient factors were used to run the model except $T$, and $P$, respectively. In the FixT simulation run, $T$ of the year 1900 (i.e., the average during 1901–1930) was used every year during 1901–2008; while in the FixP experiment, $P$ of the year 1900 (the average during 1901–1930) was used during the simulation period. The differences between simulation results of experiment Base and FixT represent effects of transient $T$ on water fluxes. The differences between Base and FixP represent effects of $P$.

### 4.4. Model Parameterization and Evaluations

[22] During the development of DLEM v1.0, field observations and plant physiological data were collected to calibrate the model and evaluate model′s performance in simulating GHG emissions and water fluxes [*Ren et al*., 2007a, 2007b; *Liu et al*., 2008, 2012; *Xu et al*., 2010; *Tian et al*., 2011a, 2011b]. In DLEM v2.0, most of the parameters related to biogeochemical and plant physiological processes are the same as the previous DLEM simulations on GHG emissions over North America [*Xu et al*., 2010]. Parameters related to hydrological processes, including interception coefficients, maximum stomatal conductance, canopy resistance, and allocation parameters, have been recalibrated due to the changes in the model structure and equations. The China sites for model calibrations can be found in *Liu et al*. [2012], and the sites over North America can be found in prior publications using DLEM [e.g., *Tian et al*., 2010a, 2010b; *Xu et al*., 2010].

[23] In the figures and tables of this paper, the long-term trend was quantified by the linear regression coefficient between simulated variables and the year. The significance was determined by testing the null hypothesis that the linear regression coefficient was not different from zero. A significance level of 0.05 was used to identify significant trends.

#### 4.4.1. Model Evaluations on ET

[24] To verify ET simulations, the simulated results were compared with observations from 20 Ameriflux networks sites (Table 3), which mainly cover the period of 2001–2006 (ftp://cdiac.ornl.gov/pub/ameriflux/data/Level4/All-Sites/; http://daac.ornl.gov/FLUXNET/fluxnet.shtml). The observed latent energy flux has been converted to water equivalent using the algorithm suggested by the AmeriFlux data support system [*Henderson-Sellers*, 1984]. Generally speaking, the model captures the magnitude of annual ET and variations across most biome types reasonably well (coefficient of determination $R^2 = 0.5$ and the root-mean-square error (RMSE) = 116 mm $yr^{-1}$), but it still has some large biases over a few stations (Figure 3). The mismatch of vegetation type between model input and the real vegetation type may cause large deviations between model results and observations. For example, the eddy flux tower in Brookings is set on a pasture land, but the dominant LC in this reconstructed historical land use data at this site is non-irrigated corn (Table 3). Another reason for these model-data biases might be that the footprint of eddy flux observations (around 1 km in radius) is much smaller than model resolution (roughly 9.3 km), and the local meteorological conditions may not reproduce the coarse climate data of the model input. The energy closure issue in the eddy flux ET observations could also produce biases between modeled results and observations [*Foken*, 2008].

#### 4.4.2. Model Evaluations on Streamflow

[26] To evaluate model performance in reproducing the magnitude and interannual variability of river discharge,

**Table 2.** Simulation Experiments

| Name | Changing Environmental Factors | Objective |
|---|---|---|
| Climate only | Climate change | To quantify effects of climate change on water fluxes |
| Land use only | Land use conversions; nitrogen fertilization | To quantify effects of land use change on water fluxes |
| FixT | Land use, nitrogen deposition, increasing atmospheric $CO_2$, and other climate factors except temperature | To quantify effects of changing temperature on water fluxes through interaction with other environmental factors |
| FixP | Land use, nitrogen deposition, increasing atmospheric $CO_2$, and other climate factors except precipitation | To quantify effects of changing precipitation on water fluxes through interaction with other environmental factors |
| Base | Land use, nitrogen deposition, increasing atmospheric $CO_2$, and climate | To quantify variations of water fluxes under impacts of multienvironmental factors |

long-term historical records were collected. Three major data sources were used for model evaluations: the Global River Discharge Database (RIVDIS v1.1) (http://www.rivdis.sr.unh.edu/) [*Vorosmarty et al*., 1998], the reconstructed Global River Flow and Continental Discharge Dataset from *Dai et al*. [2009, hereinafter referred to as Dai], and the Hydro-Climatic Data Network (HCDN) Streamflow Data Set from U.S. Geological Survey (USGS) [*Slack et al*., 1993]. The criteria for selecting sites for model evaluations are that the delineated river basin should be at least 1000 grid cells (5 arc min) and its derived basin area should be within 10% bias from the recorded basin area of these original data sources. In total, 71 rivers (23 from RIVDIS, 10 from Dai, and 38 from HCDN) were selected for model-data comparisons (Figure 1 and Table 4). For evaluating modeled long-term trends in river discharge, only the HCDN data were used because they represent long-term continuous observations.

[27] Figure 4 depicts results of comparisons between modeled river discharge, runoff, and long-term trends in river discharge. The model successfully reproduced the spatial and interannual variability of river discharge across the study area with an average $R^2$ of 0.7 (Figure 4a). The runoff, which is defined as discharge/drainage area for this comparison, shows an overall good match of modeled results with observations with a $R^2 = 0.74$. Compared to simulated results on average magnitude, simulated long-term trends in river discharge has higher bias but still acceptable ($R^2 = 0.70$) (Figures 4c and 4d). Among the 38 selected rivers, 25 (65%) had aggreement between simulated trends and observations. It needs to be pointed out that the observations are regulated discharge that has been influenced by dam construction, and currently DLEM does not consider these anthropogenic effects.

[28] To demonstrate performance of DLEM v2.0 on interannual variations over large river basins, comparisons between the simulated river discharge of the Mississippi-Atchafalaya River and gauge observations from USGS (http://toxics.usgs.gov/hypoxia/mississippi/flux_ests/delivery/index.html) (data available period: 1968–2008) and reconstructed long-term river discharge based on a land surface model (data available period: 1928–2005) [*Dai et al*., 2009] were conducted. It is encouraging that the model reasonably captures the interannual variations and long-term trend of the river discharge for the Mississippi River during the past 80 years (Figure 5). The Nash-Sutcliffe model efficiency coefficient is 0.52 when comparing DLEM simulation results with USGS observations. Since the river discharge from MARB shares more than half of total freshwater discharge to the GOM, it is reasonable to

**Table 3.** Selected AmeriFlux Eddy Flux Towers for Model Verifications

| Site | Abbreviation | State | Latitude | Longitude | Vegetation Type (IGBP Classification) | DLEM Classification[a] |
|---|---|---|---|---|---|---|
| ARM SGP Main | ARM | OK | 36.61 | −97.49 | Grassland | 100% G3 |
| Atqasuk | ATQ | AK | 70.47 | −157.41 | Grassland | 71% HW; 29% Tundra |
| Bondville | BON | IL | 40.01 | −88.29 | Cropland | 100% croplands |
| Brookings | BRO | SD | 44.35 | −96.84 | Cropland (Pasture) | 80% croplands; 17% G3 |
| Fort Peck | FPE | MT | 48.31 | −105.10 | Grassland | 100% grassland |
| Harvard forest | HAR | MA | 42.54 | −72.17 | Mixed Forest | 96% TBDF; 4% TNDF |
| Howland forest main | HOW | ME | 45.20 | −68.74 | Mixed Forest | 97% TNDF; 3% TBDF |
| Lost Creek | LOS | WI | 46.08 | −89.98 | Deciduous broad-leaf forest | 47% TeWW; 20% TBDF |
| Metolius intermediate pine | MET | OR | 44.45 | −121.56 | Evergreen needle-leaf forest | 96% TNEF; 4% DS |
| Missouri Ozark | MIS | MO | 38.74 | −92.20 | Deciduous broad-leaf forest | 96% TBDF |
| Morgan Monroe State Forest | MOR | IN | 39.32 | −86.41 | Deciduous broad-leaf forest | 100% TBDF |
| Niwot Ridge | NIW | CO | 40.03 | −105.55 | Evergreen needle-leaf forest | 76% TNEF |
| Sky Oaks Old | SKY | CA | 33.37 | −116.62 | Woody Savannas | 100% TNEF |
| Sylvania wilderness | SYL | MI | 46.24 | −89.35 | Mixed forest | 70% TNEF; 20% TBDF |
| Tonzi ranch | TON | CA | 38.43 | −120.97 | Woody savannas | 54% DS; 22% TNEF |
| UMBS | UMB | MI | 45.56 | −84.71 | Deciduous broad-leaf forest | 37% TNEF; 28% TBDF |
| Vaira ranch | VAR | CA | 38.41 | −120.95 | Woody savannas | 29% TNEF; 25% DS |
| Walker branch | WAL1 | TN | 35.96 | −84.29 | Deciduous broad-leaf forest | 87% TBDF; 3% TNDF |
| Walnut River | WAL2 | KS | 37.52 | −96.86 | Grassland | 58% G3 |
| Willow Creek | WIL | WI | 45.81 | −90.08 | Deciduous broad-leaf forest | 39% TBDF; 33% TWW |

[a]The percentage: % vegetated area in 5 arc min grid in the year 2000, and the remnant percentage is cropland. DS, deciduous shrub; ES, evergreen shrub; HW, herbaceous wetland; TBDF, temperate broadleaf deciduous forest; TeWW, temperate woody wetland; TNDF, temperate needleleaf deciduous forest; TNEF, temperate needleleaf evergreen forest.

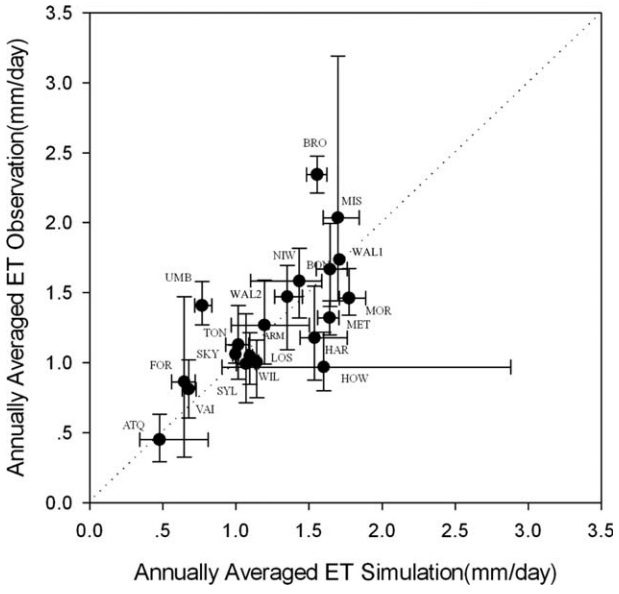


**Figure 3.** Plot of simulated mean annual ET versus observations from eddy flux towers.

conclude that simulated results are able to represent the history of freshwater discharge to the GOM during the last century.

## 5. Results

### 5.1. Land Use Change During 1901–2008

[29] The study area has experienced substantial changes in land use since the last century. Cropland increased by 41.7%, or 427,735 km$^2$, during 1901–2008, and the peak occurred in the middle of the 1980s. During the same period, forest area decreased by 1.4%, or 21,604 km$^2$ and impervious surface increased by 2.5 folds, or 27,241 km$^2$, due to urbanization. Different types and intensities of land use conversions were unevenly distributed across the drainage basins of the GOM. The cropland expansions mainly occurred in the west, while reforestation occurred in the east (Figure 6a). In the study area, most subbasins have a significant increase in cropland area and decrease in forest area or other types. Only EC, UOH, and LOH subbasins show a trend of reforestation over the cropland area (Figure 6b). Most of the land use conversions happened during the first half of the 20th century (Figure 6b). For example, cropland area increased by 210,000 and 61,000 km$^2$ in the MARB and TB basins during 1901–1950, respectively (Figure 6b). In the WSC, the cropland expansion and deforestation continued through the last hundred years (Figures 6a and 6b).

### 5.2. Interannual Variations and Long-Term Trends in Climate and Water Fluxes

#### 5.2.1. Changes in Climate and ET

[30] In the past 108 years, our study area experienced substantial climate change. According to the reconstructed historical climate data, the annual total $P$ had no significant trend during 1901–2008 within the GOM drainage basin as a whole, despite large spatial heterogeneity across the study area (Figure 7d). The increasing $P$ mainly occurred in the northern part of the MARB such as the UMS and UOH during 1901–2008 (Figure 8). During the most recent 30 years of the simulation, $P$ increased over the central part of the MARB and upstream area of the UMO (Figure 8) and decreased in the EC, LOH, and WSC (Figure 9d). The mean annual $T$ showed a significant increase by 0.49°C during 1901–2008 (Figure 7d). Again, different regions experienced different changes in $T$ across the study area. For instance, the northern coastal area of the GOM had decreases in $T$ compared with increases in all other areas during 1901–2008 (Figure 8). During 1979–2008, however, almost everywhere in the study area there was a substantial warming trend and the overall temperature increased by 0.9°C (Figures 7d, 8, and 9e).

#### 5.2.2. Changes in ET

[31] Water fluxes exhibited significant variations in response to environmental changes in the GOM drainage basin. The average estimated ET was $554.4 \pm 46.6$ mm yr$^{-1}$ (95% confidence interval), which is roughly 73% of annual $P$. Simulation results indicated a significant downward trend ($p < 0.05$) in ET by 15 mm yr$^{-1}$ century$^{-1}$ during the last 108 years (Figures 7a and 8). However, large decadal fluctuations dominated in this long time period (Figure 7a). ET declined in the west of the GOM drainage basin and southern United States, while there were increases in the upper MARB, such as the UMS and the UOH, and the west coast of the GOM during 1901–2008 (Figure 8). In recent decades, ET shows a conversion from a downward trend starting in the mid-1970s to an upward trend (Figure 7a). In the recent 30 years, all subbasins of the MARB, EC, and TB showed increasing ET, and only RGB and WSC show negative ET trends (Figures 8 and 9a).

#### 5.2.3. Changes in Runoff

[32] The simulated mean annual $R$ (includes surface runoff and baseflow) is $201.4 \pm 62.8$ mm (95% confidence limits) in the GOM drainage basin. Within the study area as a whole, $R$ showed no significant trend during 1901–2008 (Figure 6). Similarly with ET, $R$ showed large decadal variations through the last century and peaks were located in the 1940s, 1970s, and the beginning of the 1990s (Figure 7b). Compared with ET, $R$ showed much larger spatial variations in its long-term trends during 1901–2008 (Figure 8). With the exception of the central MARB and the Southern Mexico basins, most places had significant decrease in runoff during the last century (Figure 8). Comparing with 1901-1978, the EC, LOH, LMS, and WSC show substantial decrease in the recent 30 years (Figures 8 and 9b).

#### 5.2.5. Changes in Runoff/Precipitation Ratio

[33] The temporal variations of ET, $R$, and $P$ have significant correlations with each other ($p < 0.05$ for all correlations) (Figure 7). Taking this study region as a whole, the $R/P$ ratio shows no significant trend over the study period (Figure 7c). However, this is a result of a balance between regions with trends of different signs. The $R/P$ ratio decreased substantially in most subbasins of the MARB (e.g., UMO, LMO, UOH, LOH, and LMS) (Figures 8 and 10). In the UMS, AR, RO, and WSC, the $R/P$ ratio had upward trends (Figures 8 and 10). Normally, ET mediated the responses of $R$ to the changing $P$, i.e., ET increased when $P$ decreased, which would moderate the increase of $R$, and vice versa. However, there were some periods during which the responses of ET and $R$ were not concurrent,

**Table 4.** Average Annual Simulated and Observed River Discharge ($km^3\ yr^{-1}$) and the % Difference

| Source | Name | Longitude | Latitude | Periods of Available Data | Observed | Simulated | Difference (%) |
|---|---|---|---|---|---|---|---|
| Dai | Apalachicola | −85.25 | 29.75 | 1928/10–2006/9 | 19.6 | 28.0 | 42.9 |
| | Colorado, TX | −95.75 | 28.75 | 1919/4–1925/9, 1938/10–2006 | 2.5 | 7.1 | 184.3 |
| | Grijalva | −92.75 | 18.25 | 1947–1973, 1976–1981 | 16.9 | 20.6 | 21.6 |
| | Mississippi | −90.25 | 29.75 | 1928–2006 | 536.4 | 650.2 | 21.2 |
| | Neches | −94.09 | 30.36 | 1904/8–1906, 1921/4–1999/9 | 5.6 | 9.4 | 67.0 |
| | Nueces | −97.86 | 28.04 | 1939/9–1999/9 | 0.6 | 2.2 | 241.5 |
| | Pascagoula | −88.72 | 30.98 | 1930/10–1999/9 | 9.0 | 12.8 | 41.9 |
| | Sabine | −93.74 | 30.30 | 1924/10–1999/9 | 7.5 | 9.4 | 25.6 |
| | Suwannee | −82.93 | 29.96 | 1931/7–1999/9 | 6.4 | 13.3 | 110.0 |
| | Trinity | −94.85 | 30.42 | 1924/5–1999/9 | 7.0 | 10.2 | 45.3 |
| HCDN (HydroClimatic Data Network) | Apalachicola River at Chattahoochee, FL | −84.86 | 30.70 | 1929–1988 | 19.8 | 24.9 | 26.1 |
| | Beaver River at Beaver, OK | −100.52 | 36.82 | 1938–1958 | 0.1 | 0.8 | 513.1 |
| | Big Dry Creek near Van Norman, MT | −106.36 | 47.35 | 1940–1988 | 0.0 | 0.1 | 100.5 |
| | Choctawhatchee River near Bruce, FL | −85.90 | 30.45 | 1931–1988 | 6.3 | 7.8 | 24.4 |
| | Colorado River at Ballinger, TX | −99.95 | 31.73 | 1940–1952 | 0.3 | 2.8 | 719.0 |
| | East Fork White River at Shoals, Ind. | −86.79 | 38.67 | 1924–1988 | 4.8 | 5.7 | 17.3 |
| | Escambia River near Century, FL | −87.23 | 30.97 | 1935–1988 | 5.6 | 7.0 | 25.6 |
| | Flint River at Bainbridge, GA | −84.58 | 30.91 | 1929–1954 | 7.8 | 9.9 | 27.4 |
| | Frio River near Derby, TX | −99.14 | 28.74 | 1916–1988 | 0.1 | 0.5 | 300.3 |
| | G Miami R at Hamilton OH | −84.57 | 39.39 | 1930–1988 | 2.9 | 3.2 | 9.7 |
| | Gasconade River at Jerome MO | −91.98 | 37.93 | 1905–1988 | 2.3 | 2.7 | 15.4 |
| | Kaskaskia River at Carlyle, IL | −89.36 | 38.61 | 1909–1966 | 1.7 | 2.1 | 19.7 |
| | Kaskaskia River at New Athens, IL | −89.88 | 38.33 | 1910–1966 | 3.2 | 3.7 | 14.0 |
| | Little Missouri River at Marmarth, ND | −103.92 | 46.30 | 1939–1988 | 0.3 | 0.3 | −13.4 |
| | Little Missouri River near Watford City, ND | −103.25 | 47.59 | 1935–1988 | 0.5 | 0.4 | −20.6 |
| | Llano River at Llano, TX | −98.67 | 30.75 | 1944–1988 | 0.3 | 0.6 | 76.1 |
| | Mississippi River near Arkansas City, ARK | −91.24 | 33.56 | 1929–1980 | 494.7 | 512.2 | 3.5 |
| | Mississippi River at Clinton, IA | −90.25 | 41.78 | 1902–1988 | 41.6 | 37.4 | −10.2 |
| | Mississippi River at Keokuk, Iowa | −91.37 | 40.39 | 1902–1988 | 57.7 | 55.9 | −3.1 |
| | Mississippi River at Memphis, Tenn. | −90.07 | 35.13 | 1934–1988 | 431.4 | 417.4 | −3.2 |
| | Mississippi River at Vicksburg, MS | −90.91 | 32.31 | 1932–1988 | 523.4 | 545.2 | 4.2 |
| | N Platte R Ab Seminoe Res near Sinclair Wyo | −107.06 | 41.87 | 1940–1988 | 1.0 | 0.6 | −38.5 |
| | Neches River At Evadale, TX | −94.09 | 30.36 | 1908–1964 | 5.6 | 8.4 | 48.6 |
| | Neosho R near Iola, KS | −95.43 | 37.89 | 1902–1962 | 1.5 | 1.7 | 11.5 |
| | Nueces River near Three Rivers, TX | −98.18 | 28.43 | 1926–1983 | 0.8 | 2.2 | 194.0 |
| | Nueces River near Tilden, TX | −98.56 | 28.31 | 1916–1988 | 0.4 | 1.0 | 156.5 |
| | Pease River near Childress, TX | −100.07 | 34.23 | 1925–1988 | 0.1 | 0.4 | 658.5 |
| | Rio Grande below Taos Junction Bridge near Taos, NM | −105.75 | 36.32 | 1929–1988 | 0.7 | 1.2 | 75.8 |

**Table 4.** (continued)

| Source | Name | Longitude | Latitude | Periods of Available Data | Observed | Simulated | Difference (%) |
|---|---|---|---|---|---|---|---|
| | Rock River at Afton, WI | −89.07 | 42.61 | 1915–1988 | 1.7 | 1.8 | 7.2 |
| | Sabine River near Ruliff, TX | −93.74 | 30.30 | 1905–1966 | 7.5 | 9.1 | 20.7 |
| | Saline R at Tescott, KS | −97.87 | 39.00 | 1920–1964 | 0.2 | 0.4 | 67.7 |
| | Scioto R at Higby, OH | −82.86 | 39.21 | 1931–1988 | 4.1 | 3.9 | −5.1 |
| | Suwannee River at Branford, FL | −82.93 | 29.96 | 1932–1988 | 6.3 | 13.2 | 110.3 |
| | Tombigbee River at Demopolis L&D Near Coatopa AL | −87.88 | 32.52 | 1929–1988 | 20.6 | 25.0 | 21.6 |
| | Wabash River at Lafayette Ind | −86.90 | 40.42 | 1924–1988 | 5.8 | 5.0 | −13.5 |
| | Wabash River at Mt. Carmel, IL | −87.75 | 38.40 | 1928–1988 | 24.6 | 25.4 | 3.6 |
| | White River at Newberry, Ind. | −87.01 | 38.93 | 1929–1988 | 4.2 | 5.6 | 33.4 |
| | White River at Petersburg Ind. | −87.29 | 38.51 | 1929–1988 | 10.5 | 11.2 | 6.2 |
| RIVDIS (The Global River Discharge Database) | Brandford, Florida | −82.93 | 29.95 | 1965–1984 | 6.8 | 13.3 | 93.8 |
| | Chattahoochee, Florida | −84.86 | 30.70 | 1930–1984 | 19.8 | 25.9 | 31.0 |
| | Claiborne, Alabama | −87.51 | 31.53 | 1931–1976, 1980–1983 | 29.6 | 32.9 | 10.9 |
| | Culbertson, Montana | −104.46 | 48.11 | 1965–1967, 1969–1984 | 46.3 | 41.9 | −9.4 |
| | Evedale, Texas | −94.10 | 30.35 | 1965–1984 | 11.0 | 9.1 | −17.6 |
| | Little Rock, Arkansas | −92.26 | 34.75 | 1928–1984 | 21.5 | 26.9 | 24.8 |
| | Little Rock, Arkansas | −91.45 | 34.78 | 1965–1969 | 4.7 | 9.1 | 92.4 |
| | Little Rock, Arkansas | −90.90 | 32.31 | 1965–1982 | 73.1 | 87.3 | 19.5 |
| | Louisville, Kentucky | −85.78 | 38.28 | 1965–1983 | 33.5 | 51.5 | 53.8 |
| | Mathis, Texas | −97.86 | 28.03 | 1965–1984 | 108.7 | 89.2 | −17.9 |
| | Merrill, Missisippi | −88.73 | 30.98 | 1931–1984 | 0.8 | 2.2 | 181.1 |
| | Metropolis, Illinois | −88.73 | 37.15 | 1928–1984 | 8.9 | 12.5 | 40.3 |
| | Monroe, Louisiana | −92.13 | 32.50 | 1965–1975 | 234.1 | 220.3 | −5.9 |
| | Monroe, Louisiana | −91.43 | 38.71 | 1898–1987 | 17.4 | 22.9 | 31.2 |
| | Monroe, Louisiana | −90.25 | 41.78 | 1965–1984 | 26.3 | 26.1 | −0.6 |
| | Mt Carmel, Illinois | −87.75 | 38.40 | 1965–1983 | 36.3 | 37.8 | 4.1 |
| | Nebraska City, Nebraska | −95.83 | 40.66 | 1965–1983 | 6.5 | 9.8 | 52.1 |
| | Romayor, Texas | −94.85 | 30.43 | 1969–1984 | 6.5 | 9.0 | 38.5 |
| | Ruliff, Texas | −93.75 | 30.30 | 1965–1984 | 18.7 | 16.6 | −11.2 |
| | Samaria | −93.29 | 17.97 | 1976–1981 | 12.3 | 6.3 | −49.3 |
| | Sidney, Montana | −104.16 | 47.61 | 1965–1984 | 6.2 | 14.4 | 132.0 |
| | Tulsa, Oklahoma | −96.00 | 36.15 | 1965–1967, 1969–1978, 1980–1984 | 536.3 | 548.2 | 2.2 |
| | Wharton, Texas | −96.10 | 29.30 | 1965–1984 | 2.3 | 7.0 | 198.2 |

thus potentially triggering abnormal $R/P$. Trends in $R/P$ normally followed with the trends in $P$. With decreasing $P$ in the EC, LOH, RGB, and WSC during 1979–2008, the $R/P$ also decreased (Figures 8 and 9), which means these regions became much drier due to increased ET loss.

### 5.3. Seasonal Patterns of Water Fluxes

[34] Simulation results indicated a statistically significant ($p < 0.05$) decrease of ET during the winter season (December–February) and a significant increasing trend in $R$ during the fall season (September–November) during 1901–2008 over the study area as a whole (Table 5). ET showed the largest decrease by 5 mm season$^{-1}$ century$^{-1}$ in the winter compared with other seasons, which was corresponding with substantial decreases in $P$ during winter season (Table 5). Runoff had a substantial increase by 8.6 mm season$^{-1}$ century$^{-1}$ in the autumn (Table 5). During the recent 30 years, both $R$ and ET decreased in the winter and the spring due to a large decrease in $P$ (Table 5).

### 5.4. Effects of Changing T, P, and Land Use on Long-Term Trends of Water Fluxes

[37] Among the environmental factors, the climate variation was the dominant factor controlling the temporal and spatial patterns of ET and $R$ anomalies during 1901–2008, which could explain 99% of interannual variations of ET (Figure 7). However, for the long-term trend of ET, land use change contributed approximately the same as climate change did. For example, ET was reduced by 9.1 and 10.5 mm yr$^{-1}$ century$^{-1}$ due to land use and climate change during 1901–2008, respectively (Table 6). The net contributions from other environmental factors was relatively small (i.e., around 4.4 mm yr$^{-1}$ century$^{-1}$) (Table 6). Among the climate factors, $P$ played a dominant role in determining interannual variations of ET (Figure 7a). Combined with other factors, long-term changes in $P$ caused a decrease in ET of 9 mm yr$^{-1}$ century$^{-1}$over the GOM drainage basin during 1901–2008. In the past 30 years, effects of $P$ on ET were much larger than prior periods (Table 6). Although $T$

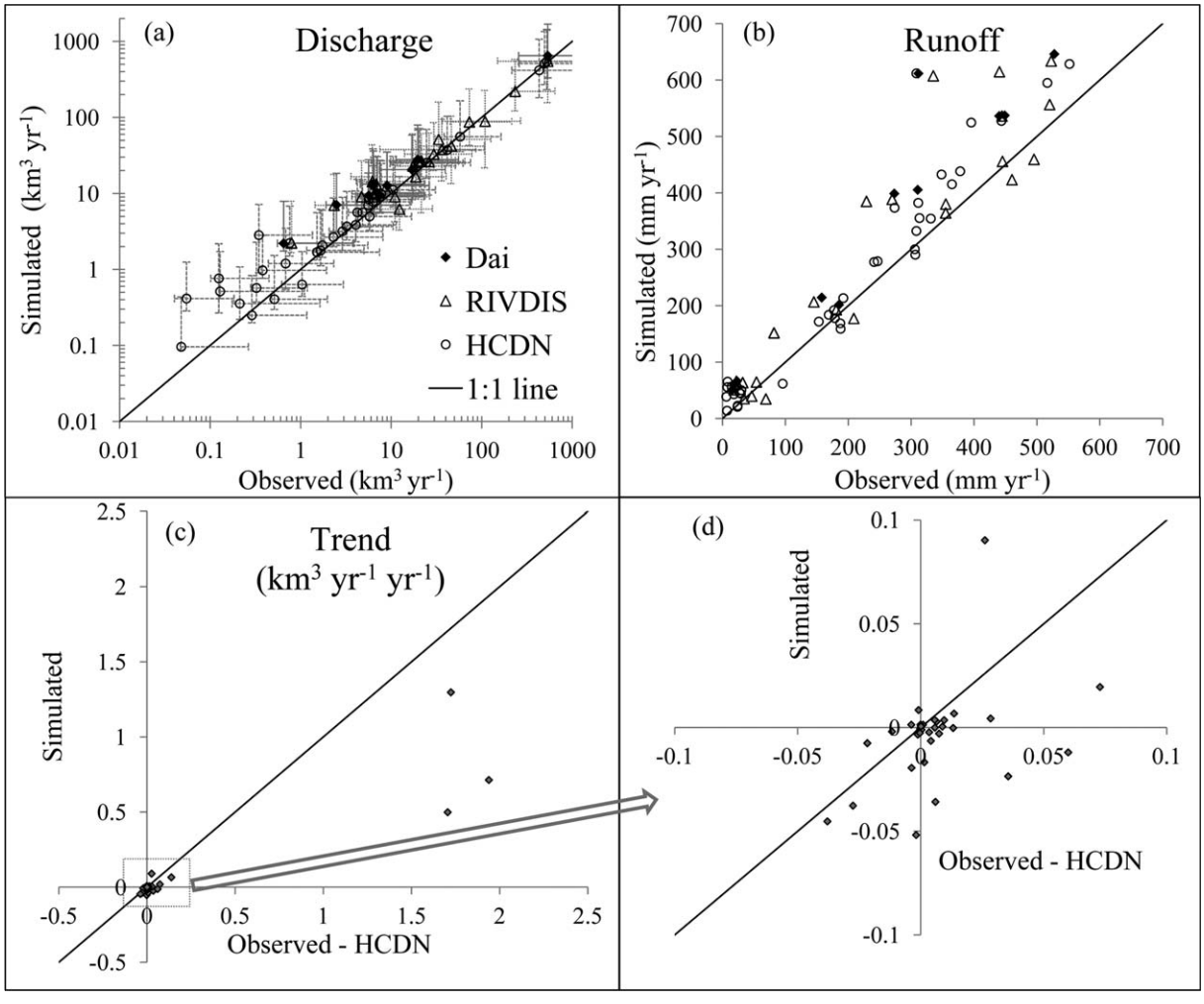


**Figure 4.** Plots of simulated river discharge and runoff vs observations. (a) Mean annual river discharge; (b) mean annual runoff; and (c and d) long-term trend.

can change ET, this change is mostly moderated by *P*. For instance, in the beginning of the 1950s and the period around 2000, the higher *T* tended to result in higher potential ET, but the real ET was limited by lower *P* (Figures 7a and 7d). A similar pattern on the global level was reported by *Jung et al*. [2010]. Overall, the recent warming during 1979–2008 increased ET by a rate of 12.8 mm $yr^{-1}$ $century^{-1}$ in the GOM drainage basin.

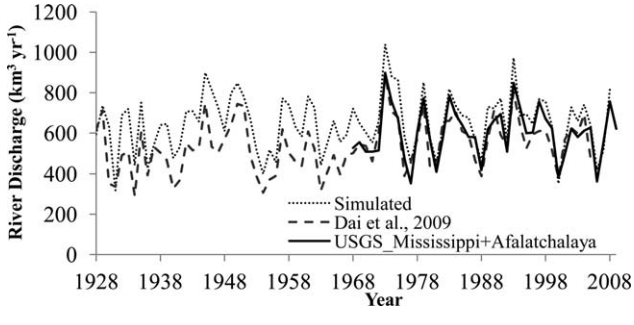


**Figure 5.** Simulated river discharges versus reconstructed historical discharge [*Dai et al*., 2009] and USGS observations.

[41] As for *R*, climate variations could account for more than 99% of its fluctuations (Figure 7b). Only land-use change significantly altered the long-term trend of *R* and the total effects of climate were small during the last 108 years. However, the effect of *P* on *R* was substantial during short-term periods such as the recent 30 years. Climate change (decreasing *P* and increasing *T* and changes in other factors) reduced *R* by 32 mm $yr^{-1}$ during the 30 year period (Table 6). As for the *R*/*P* ratio, land use change caused a consistent increase it over the last 108 years when taking the GOM drainage basin as a whole (Table 6), while the climate change decreased the *R*/*P* ratio, particularly over the last 30 years.

[42] The impacts of environmental change on hydrological processes vary immensely across the GOM drainage basin. Figures 8 and 11 indicate that climate change generally controls the spatial patterns of long-term trends in ET. However, land use change does act as a dominant role in shaping the long-term trend of ET in certain places such as the upper basin of the Ohio River and the deforestation area in the WSC (Figure 11). In the UMS and UOH, the land use and climate change both have a positive effect on ET, thus they cause substantial increases of ET in these regions (Figures 10 and 11).

[43] In the water-limited area such as the west of the GOM drainage basin (RGB, TB, RO, AR, LMO, and

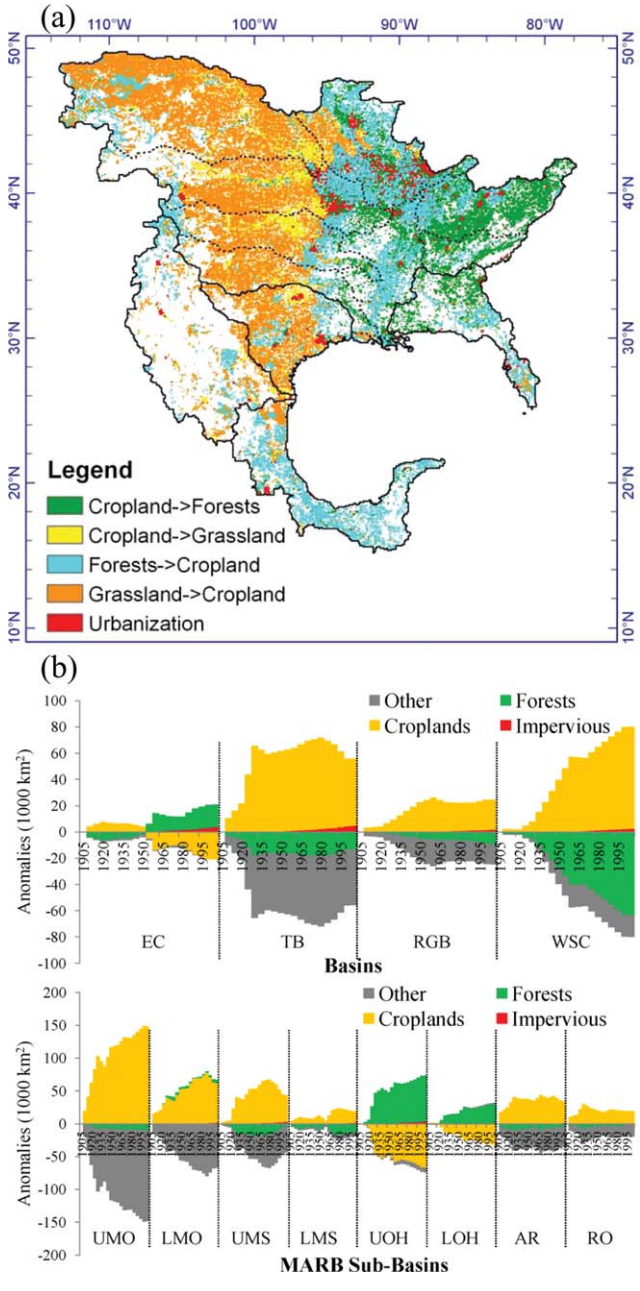


**Figure 6.** Land use change in the first and second half 20th century in each subbasin. (a) Spatial distribution (the color of each grid cell represents the dominant land use conversion type that has at least 0.5% change in total area of the grid cell) and (b) relative change from the start year 1901 for each subbasins.

UMO), trends in ET are mainly controlled by the available *P* (Figures 8 and 10). The decrease of *P* in this water-limited region caused ET to decrease even though *T* rose concurrently (Figure 8). In the upper Mississippi River Basin (UMS and UOH), ET was both energy limited and water limited, so the increasing *T* and *P* accelerated ET during the last 108 years (Figures 10 and 11). In the northern coastal area of the GOM, ET was mainly energy limited and the cooling trend in this region caused a decrease in ET even with increasing *P* during 1901–2008 (Figures 8 and 10). The combined effects of changes in *T*, *P*, and land use were revealed by the long-term trends in the *R*/*P* ratio (Figure 8). The widely distributed deforestation in WSC increased the *R*/*P* ratio by 30% during 1901–2008. The reforestation area in the Appalachian Mountains and the cropland abandonments might explain the decrease of *R*/*P* ratio in this region. In almost all other subbasins, land use change increased the *R*/*P* ratio (Figure 10).

### 5.5. Changes in Freshwater Discharge

[44] According to simulated results, the average water flow to the GOM from the drainage area was about 1,100 $km^3\ yr^{-1}$. The water discharge from the MARB contributed around 60% of the total water yield (655 $km^3\ yr^{-1}$) (Table 7). The second and third contributors are the EC (18%) and the WSC (14%), respectively. The interannual variations of total freshwater discharge to the GOM are mainly regulated by the MARB as depicted in Figure 12. No significant long-term trend in total freshwater discharge to the GOM is detected for this century-long period (Table 7 and Figure 12). During the period from the mid-1970s to the beginning of 21st century, however, a significant decreasing trend with a slope of 13% is estimated by the model (Figure 12). The fluctuations of freshwater discharge from these basins have some common patterns. However, they represent different signs and magnitude in long-term trends (Figure 12). Subbasins UMO, EC, and RGB all have a more than 5% decrease during 1979–2008 than the prior period, while the UMS, AR, RO, and TB have substantial increase in freshwater discharge (Table 7).

[46] From *Dai et al.*'s [2009] global observational river discharge data base, 32 rivers that flow into the GOM were selected and the missing data were filled with multiyear mean monthly flow observations for a comparison with DLEM results. Figure 12 illustrates that the modeled estimation is very close to the observed flow at both interannual variations and decadal trends. The simulated freshwater discharge to the GOM is larger than Dai et al.'s reconstructed records by 32.5% during 1928–2006 (Figure 12). The primary reason for this difference is that total GOM drainage area (5.37 million $km^2$) in these simulations is larger than the drainage area of these 32 rivers (4.31 million $km^2$) by 25.7%. Considering the difference in drainage area, the simulated average annual discharge is about 6% larger than observations. One reason for this overestimation is that DLEM does not consider the effect of dam constructions and so underestimates the water loss through ET. The second reason is that the reconstructed records only take the sample from the river gauges, not including the subsurface flow from land to the ocean. The fluctuations and long-term changes in water flow, as well as the accompanied nutrients exports from land to the GOM, may influence the physical and biogeochemical cycles in the ocean and coastal regions which needs further investigations [*Seitzinger et al.*, 2005; *Cai*, 2011].

## 6. Discussions

### 6.1. Comparison With Other Studies

[47] Recently, many research activities in the context of global change have been conducted to assess effects of environmental change on large-scale water resources.

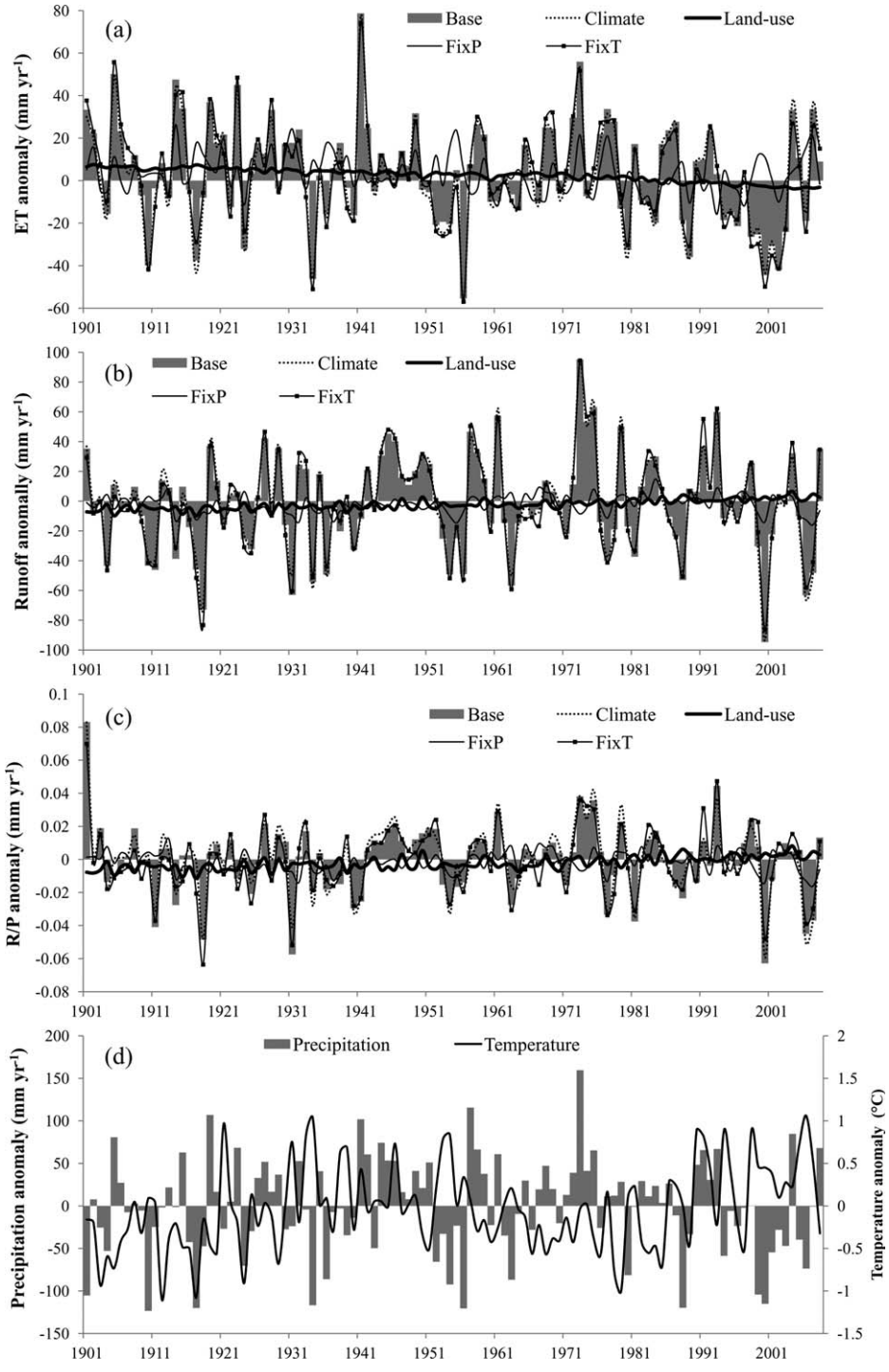


**Figure 7.** Anomalies of annual ET, runoff, precipitation, and mean annual temperature during 1901–2008. The lines in Figures 7a–7c represent simulated results from different factorial experiments. The columns in Figures 7a–7c represent simulated results from Base run (i.e., all environmental factors); the baseline is the average between 1961–1990. Each panel represents (a) ET; (b) runoff; (c) $R/P$ ratio; and (d) precipitation and temperature.

Besides land surface modeling efforts, two new methods are considered as efficient ways to estimate contemporary ET with finer spatial and temporal scales: one is the remote sensing-based estimations and the other is the upscaling method from continuous field observations [*Baldocchi et al*., 2001; *Mu et al*., 2007, 2011; *Jung et al*., 2009, 2010; *Wang et al*., 2010a, 2010b; *Zhang et al*., 2010; *Mueller et al*., 2011]. *Mueller et al*. [2011] reported differences among 41 global land ET data sets, including global GCM simulations and observations-based estimations. However, the observational data sets also have large uncertainties, which add difficulties in evaluating model simulation accuracy

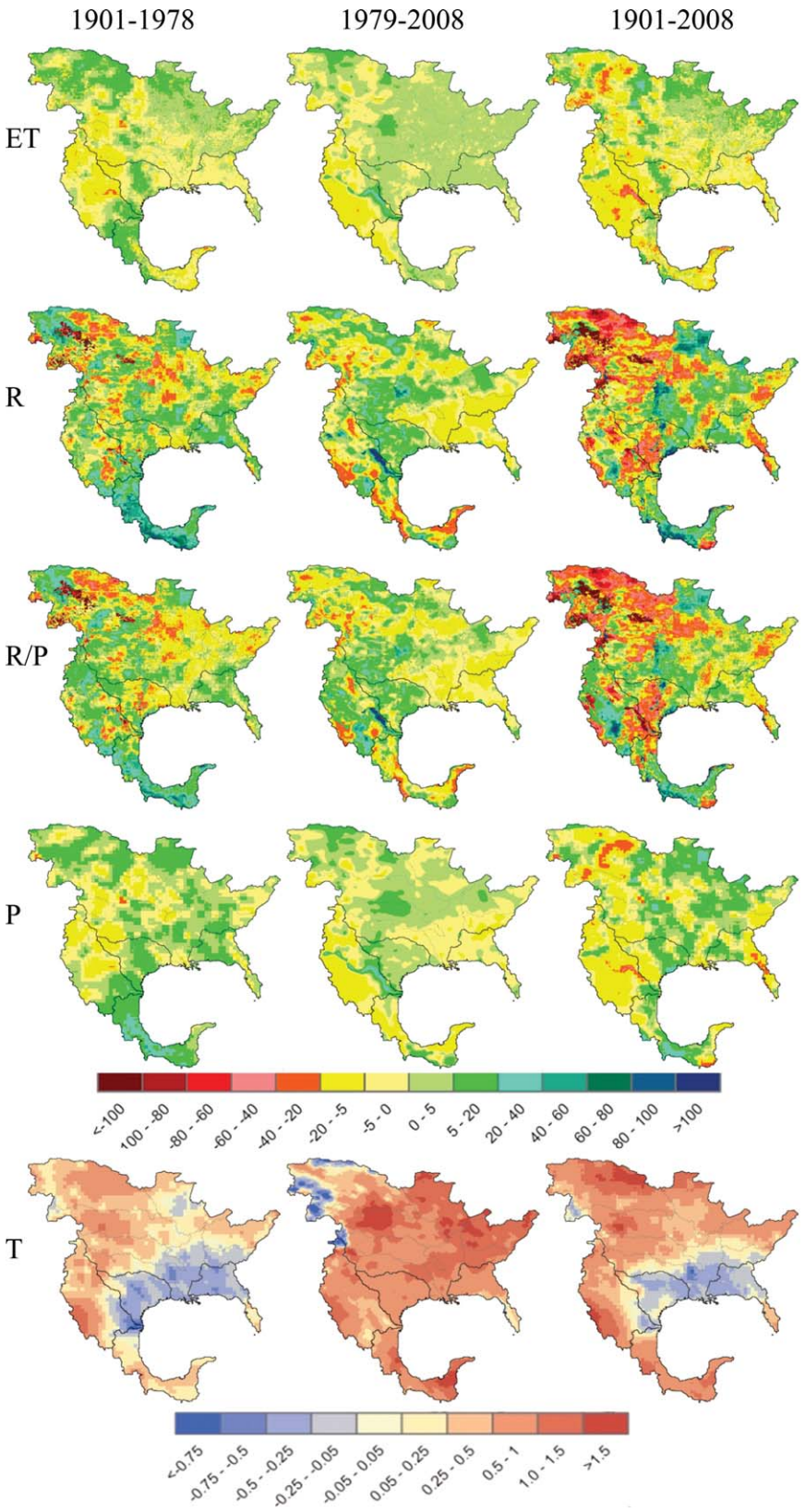


**Figure 8.** Spatial distributions of trends in annual ET, runoff ($R$), $R/P$, $P$ (precipitation), and $T$ (temperature) during periods of 1901–1978, 1979–2008, and 1901–2008. The unit for ET, $R$, $R/P$, and $P$ is the percentage rate of change during different period (base period: 1961–1990); the unit for $T$ is total change in degree Celsius per period.

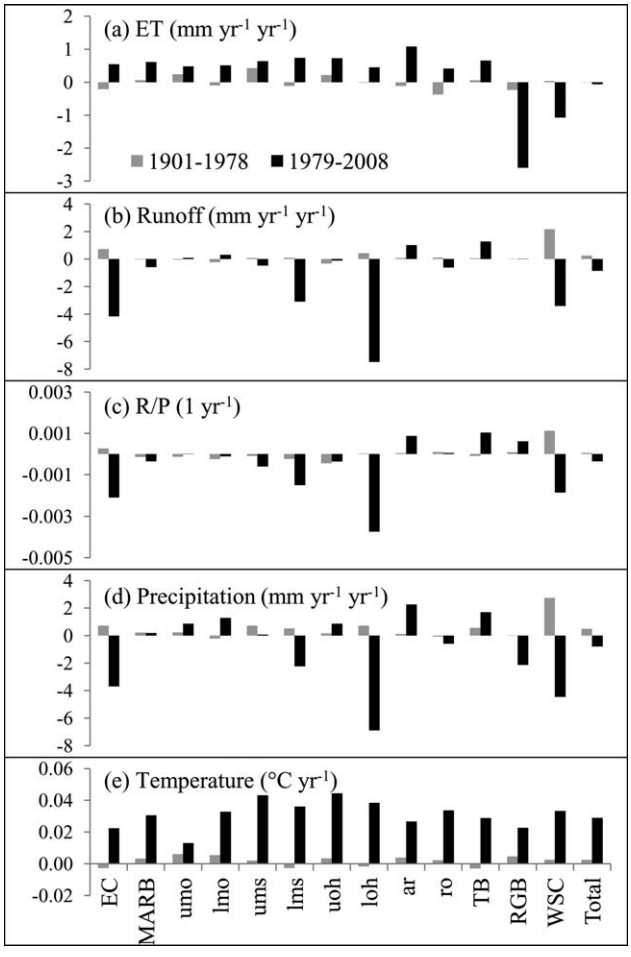


**Figure 9.** Trends in ET, runoff, *R*/*P*, precipitation, and temperature during the period of 1901–1978 and 1979–2008 over different basins. The lowercase names represent subbasins of the MARB. (a) ET; (b): runoff; (c) *R*/*P*; (d) precipitation; and (e) temperature.

and reliability [*Mueller et al*., 2011]. In spite of the uncertainties of upscaling estimations from eddy-covariance flux measurements, the upscaled products have been considered as the most reliable ET estimations in representing ET′s spatial distributions, magnitude, and long-term trend. Here, DLEM simulated results were compared with an upscaled ET estimation from FLUXNET over the period of 1982–2008, which was derived from a machine-learning algorithm (the model tree ensemble or MTE) and had a spatial resolution of half degree [*Jung et al*., 2009, 2010]. The multiyear average of estimated ET from DLEM and MTE is highly consistent as shown in Figures 13a and 13b although DLEM slightly underestimated ET in coastal areas. Furthermore, DLEM and MTE both detected decreasing trends of ET in the UMO and increasing trends in LOH, UOH, EOC, LMS, and RO (Figures 13c and 13d). However, in UMS and RGB, DLEM and MTE show opposite trends. For the period of 1992–2002, both of them detected a decline of ET but DLEM estimated a larger decrease than MTE. As to the interannual variations, DLEM and MTE had comparable results for interannual variations and magnitudes (Figure 13e). It needs to be pointed out that the MTE data sets are also modeled results with uncertainties from training data and explanatory variables [*Jung et al*., 2009].

[48] Simulated results were also compared with variable infiltration capacity (VIC) derived evaporation data for the period of 1950–1999 [*Maurer et al*., 2002]. The overlay area of these two data sets covers most of the drainage basin of the GOM except the Mexico area. These two models have close estimations the magnitude of ET and its interannual variations (Figure 14), but they have different estimations of the trend. VIC detected a significant increasing trend of ET in this period while DLEM did not (Figure 14). However, both models detected a strong decrease of ET since 1992, which MTE failed to catch (Figure 14). To quantify uncertainties and improve simulation performance in long-term trends, new global data sets from multisource can be applied as training data and evaluation base lines [*Fisher et al*., 2008; *Vinukollu et al*., 2011a, 2011b; *Pan et al*., 2012].

### 6.2. Driving Forces to the Variations of Water Fluxes to the GOM

[49] Currently, there are different opinions over long-term trend of global fresh water export from land to the ocean. As to the global scale studies, some scientists reported an increasing trend of runoff during the last century [e.g., *Labat et al*., 2004; *Gedney et al*., 2006; *Piao et al*., 2007]. This conclusion, however, is likely questionable due to the representativeness of the limited number of selected rivers as discussed in detail by *Dai et al*. [2009]. Another argument is whether land use [e.g., *Vorosmarty and Sahagian*, 2000; *Sun et al*., 2005; *Piao et al*., 2007; *Zhang et al*., 2007b] or natural factors [*Gedney et al*., 2006; *Wang et al*., 2008; *Dai et al*., 2009] dominate the long-term trends and decadal variations of water fluxes at the global scale [*IPCC*, 2007]. According to this study, it can be found that in certain places land use play major roles in variations of water fluxes, while in other places natural factors may dominate. To the policy makers, assessments on impacts of natural environmental changes and human disturbances on the water resources from local and regional scales are critical for sustainable water resource management.

[50] A few studies have reported driving force analyses on the hydroclimatic trends in the MARB [e.g., *Milly and Dunne*, 2001; *Qian et al*., 2007]. *Qian et al*. [2007] claimed that "the increase of precipitation is compensated by both runoff (65%) and evapotranspiration (38%)." However, their study did not take in account the LC change and irrigation effects on cropland ET. Uncertainties related to land surface model (namely CLM) and *P* data could also lead to bias of their estimations [*Lawrence et al*., 2007; *Qian et al*., 2007; *Oleson et al*., 2008]. For the same period of 1948–2004, DLEM resulted in a decrease of ET at a rate of $-23 \pm 32$ mm yr$^{-1}$ century$^{-1}$ and an increasing trend of *R* at a rate of $18 \pm 65$ mm yr$^{-1}$ century$^{-1}$ in the MARB. Since *P* slightly decreased by $-3 \pm 10$ mm yr$^{-1}$ century$^{-1}$, it can be concluded that the increasing *R* is primarily caused by the decreasing ET. One reasonable explanation for the discrepancy between this study and *Qian et al*. 2007′s study (by using NCEP-NCAR 1.6° global data sets) may be the differences in *P* data.

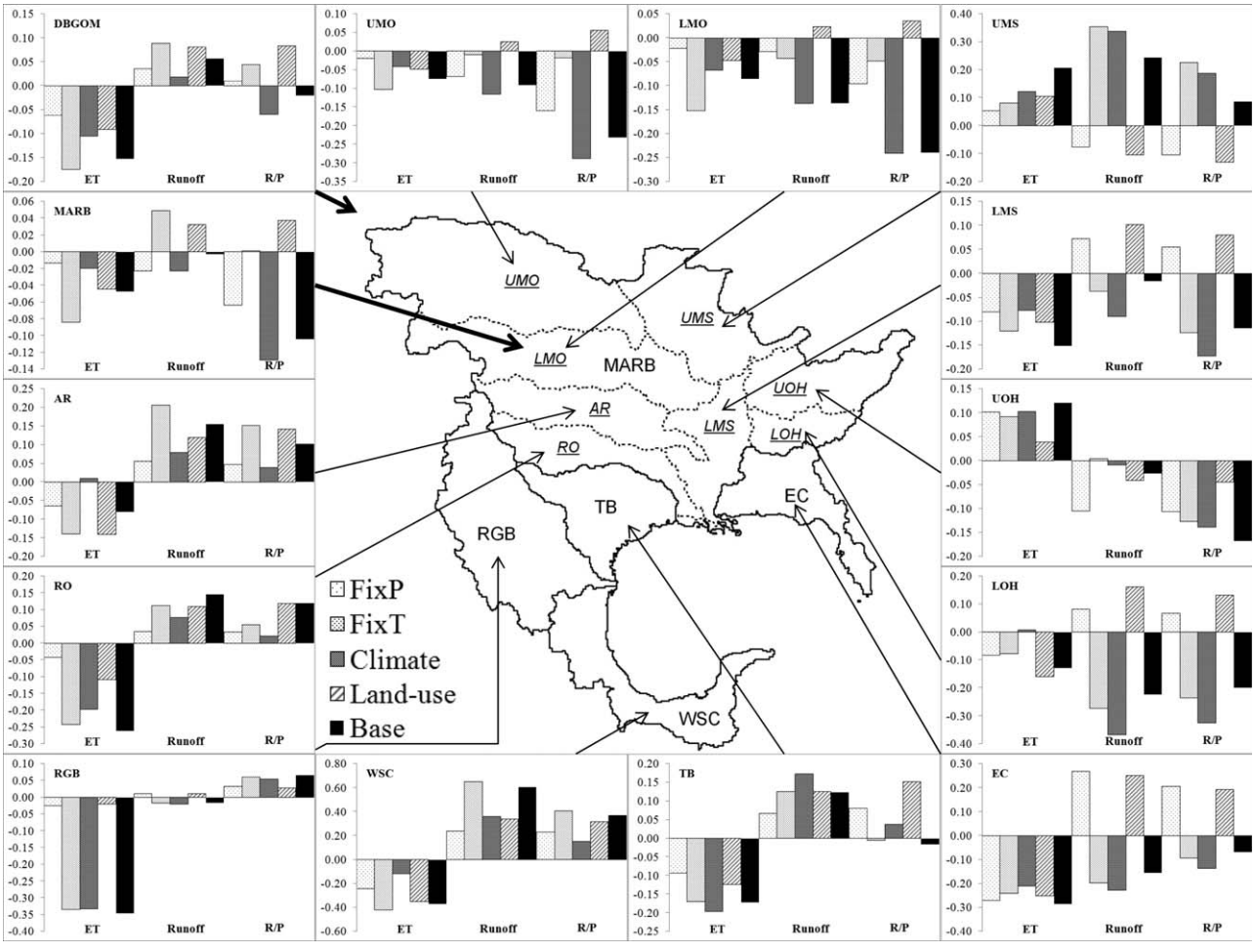


**Figure 10.** Estimated trends in annual ET, runoff, and $R/P$ during 1901–2008 driven by different combination of environmental factors over each subbasin of the GOM drainage basin. The unit for ET and runoff is mm $yr^{-1}$ $yr^{-1}$ and for $R/P$ is 0.001 $yr^{-1}$ (i.e., the $y$ axis reading multiply 0.001 to get the annual changing rate of $R/P$).

[51] Among the effects of major land use conversions on ET, urbanized area (i.e., the dominant conversion type and total change greater than 5% of grid area, as shown in Figure 6a) had the largest decrease in ET at a rate of 100 mm $yr^{-1}$ $century^{-1}$ and deforestation area had an average decrease of 28 mm $yr^{-1}$ $century^{-1}$. In the area of cropland abandonment, ET decreased by 19 mm $yr^{-1}$ $century^{-1}$ on the average. Land conversion-caused increase in ET happened only in afforestation or reforestation areas, and the magnitude was very small (2.2 mm $yr^{-1}$ $century^{-1}$) as estimated by DLEM. Since DLEM considers irrigation and fertilizer use on cropland, its conversions to forest land or grassland do not always end with increasing ET as proposed by *Sun et al*. 2005, but may possibly even decrease ET as documented by *Liu et al*. 2008. Grid cells with more than 50% changes in land use were collected, and the statistics demonstrate that that irrigated cropland abandonment generally reduce ET by 93 mm $yr^{-1}$ and nonirrigated

**Table 5.** Seasonal Trend of ET, Runoff, and Precipitation During 1901–2008[a]

| | ET (mm season$^{-1}$ century$^{-1}$) | | | Runoff (mm season$^{-1}$ century$^{-1}$) | | | Precipitation (mm season$^{-1}$ century$^{-1}$) | | | Temperature (°C century$^{-1}$) | | |
|---|---|---|---|---|---|---|---|---|---|---|---|---|
| Season | 1901–1978 | 1979–2008 | 1901–2008[a] | 1901–1978 | 1979–2008 | 1901–2008[a] | 1901–1978 | 1979–2008 | 1901–2008[a] | 1901–1978 | 1979–2008 | 1901–2008[a] |
| Winter: Dec.–Feb. | −3.4 | −28.1* | −5.1* | 2.6 | −50.1 | −1.5 | −13.1 | −190.6 | −36.9 | −0.01 | 5.85* | 0.56 |
| Spring: Mar.–May. | 3.5 | −14.5 | −3.7 | 4.2 | −27.6 | −1.5 | 24.5 | −152.2 | −10.2 | 0.39 | 2.64 | 0.68* |
| Summer: Jun.–Aug. | −2.7 | 20.8 | −2.2 | 3.8 | −0.1 | 1.8 | 11.5 | 72.9 | 7.5 | 0.79* | 1.46 | 0.60* |
| Autumn: Sep.–Nov. | 4.1 | 13.7 | −2.9 | 18.5* | −7.3 | 8.6* | 95.0 | 0.9 | 28.9 | 0.16 | 1.96 | 0.17 |
| Annual[b] | −2.8 | −38.9 | −16.0* | 28.3 | −102.8 | 3.8 | 50.6 | −147.3 | −1.6 | 0.33 | 3.81* | 0.48* |

[a]Values with an asterisk indicate significance, i.e., $p < 0.05$

[b]This "annual" is counted from December to second year's November and the start year is 1902 for the period of 1901–1978 and 1901–2008.

**Table 6.** Relative Contributions of Environmental Changes to the Linear Trend of ET and Runoff as Estimated by DLEM During 1901–2008[a]

| | ET (mm yr$^{-1}$ century$^{-1}$) | | | Runoff (mm yr$^{-1}$ century$^{-1}$) | | | Runoff/Precipitation (1 century$^{-1}$) | | |
|---|---|---|---|---|---|---|---|---|---|
| Factors | 1901–1978 | 1979–2008 | 1901–2008[b] | 1901–1978 | 1979–2008 | 1901–2008[b] | 1901–1978 | 1979–2008 | 1901–2008[b] |
| FixP | −5.4 | 46.1* | −6.1* | 4.0 | −41.0* | 3.6 | 0.002 | −0.040* | 0.001 |
| *P effects*[c] | *4.7* | *−52.5* | *−9.1* | *21.5* | *−45.4* | *2* | *0.003* | *0.004* | *−0.003* |
| FixT | −2.0 | −19.2 | −17.4* | 26.4 | −75.0 | 8.9 | 0.008 | −0.027 | 0.004 |
| *T effects*[c] | *1.3* | *12.8* | *2.2* | *−0.9* | *−11.4* | *−3.3* | *−0.003* | *−0.009* | *−0.006* |
| Climate | 1.1 | 14.8 | −10.5 | 23.8 | −105.0 | 1.8 | 0.004 | −0.062 | −0.006 |
| Land use | −6.9* | −17.2* | −9.1* | 6.5* | 13.1* | 8.1* | 0.006* | 0.013* | 0.008* |
| Base | −0.7 | −6.4 | −15.2* | 25.5 | −86.4 | 5.6 | 0.005 | −0.036 | −0.002 |

[a]Values with an asterisk indicate significance, i.e., $p < 0.05$;
[b]Because of a time interrupt in 1978–1979, the linear trend during 1901–2008 is not the same as the mathematic summary of linear trend during 1901–1978 and 1979–2008;
[c]The effects of *P* and *T* are calculated as the differences in long-term trends between base simulations (i.e., all environmental factors) and experiment of FixP and FixT, respectively. There is no significant indicator for these estimates.

cropland abandonment only reduce ET by 50 mm yr$^{-1}$ (Figure 15). Cropland expansions did not significantly increase ET in the GOM basin as a whole, but it needs to be pointed out that there are wide distributions of the range (Figure 15). The effects of land management and land conversions on large-scale water cycles need to be further investigated through integrating field observations and finer resolution hydrological models [*Andreassian*, 2004; *Jackson et al*., 2005; *Zhang and Schilling*, 2006; *Rotter et al*., 2011].

### 6.3. Model Limitations

[52] DLEM has been intensively calibrated with ET observations. *Zhang et al*. 2009 have indicated that calibrations both on ET and streamflow can significant improve the model′s capabilities in simulating regional water fluxes and streamflow simulations, particularly over ungauged basins. To enhance DLEM′s performance in seasonal streamflow, parameters related to water routing processes, such as the stream flow rate and residential times of lakes, surface and ground water reservoirs, and runoff processes

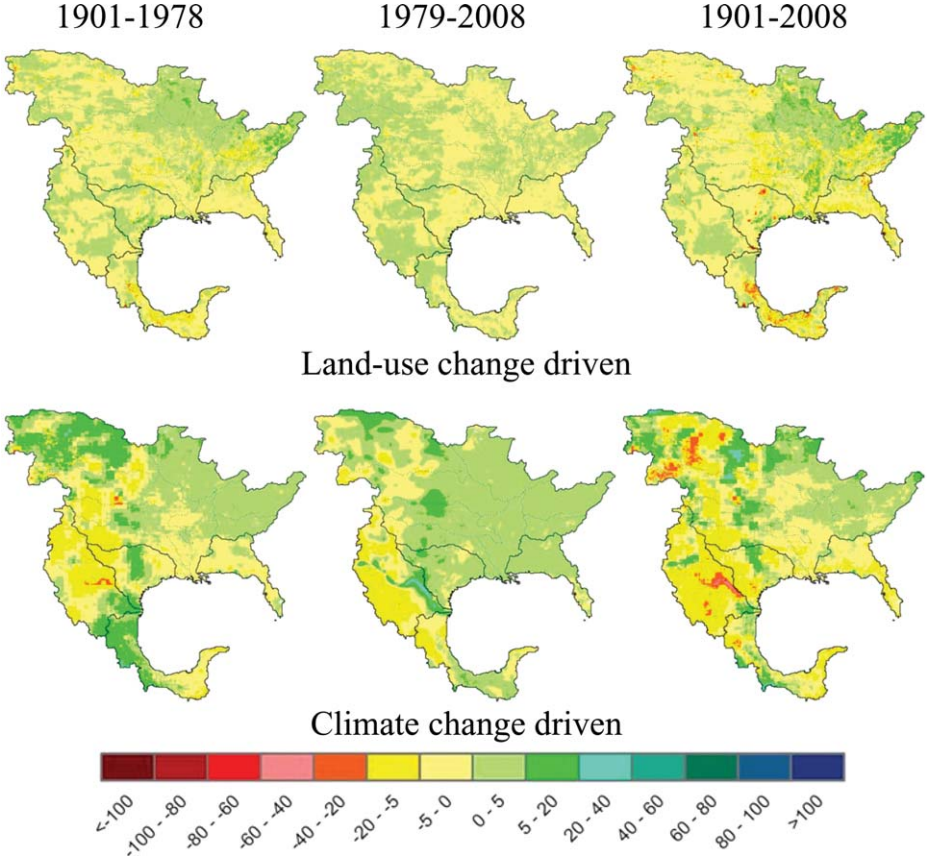


**Figure 11.** Spatial distributions of trends in ET during different periods driven by climate change and land use change (unit: the percentage rate of change per period) (base period: 1961–1990).

**Table 7.** Changes in Water Discharges of Each Subbasin During 1901–2008

| | Average annual discharge ($km^3\ yr^{-1}$) | | Change (Post-1979 vs. Pre-1979) | | Linear Trend | | | |
|---|---|---|---|---|---|---|---|---|
| | | | | | 1901–1978 | | 1979–2008 | |
| Subbasins | 1901–1978 | 1979–2008 | $km^3\ yr^{-1}$ | % | $km^3\ yr^{-1}\ yr^{-1}$ | $\%\ yr^{-1}$ | $km^3\ yr^{-1}\ yr^{-1}$ | $\%\ yr^{-1}$ |
| East Coast of the GOM (EC) | 205.92 | 194.72 | −11.20 | −5.4% | 0.26 | 0.13% | −1.48 | −0.76% |
| Mississippi-Atchafalaya River Basin (MARB) | 653.05 | 660.49 | 7.44 | 1.1% | −0.12 | −0.02% | −1.85 | −0.28% |
| Upper Missouri (UMO) | 28.19 | 22.81 | −5.38 | −19.1% | −0.03 | −0.10% | 0.04 | 0.17% |
| Lower Missouri (LMO)[a] | 62.94 | 59.98 | −2.96 | −4.7% | −0.13 | −0.20% | 0.17 | 0.28% |
| Upper Mississippi (UMS) | 81.09 | 89.59 | 8.50 | 10.5% | 0.03 | 0.04% | −0.22 | −0.25% |
| Lower Mississippi (LMS)[a] | 120.76 | 126.60 | 5.83 | 4.8% | 0.04 | 0.03% | −0.90 | −0.71% |
| Upper Ohio (UOH) | 137.71 | 140.97 | 3.26 | 2.4% | −0.12 | −0.09% | −0.05 | −0.04% |
| Lower Ohio (LOH) | 81.54 | 78.79 | −2.74 | −3.4% | 0.05 | 0.06% | −1.14 | −1.45% |
| Arkansas (AR) | 56.58 | 59.70 | 3.12 | 5.5% | 0.03 | 0.06% | 0.38 | 0.63% |
| Red and Ouachita (RO) | 56.07 | 59.26 | 3.19 | 5.7% | 0.03 | 0.06% | −0.17 | −0.28% |
| Texas Basin (TB) | 62.64 | 65.59 | 2.95 | 4.7% | 0.02 | 0.04% | 0.56 | 0.86% |
| Rio Grande Basin (RGB) | 26.12 | 24.61 | −1.51 | −5.8% | 0.01 | 0.03% | 0.00 | −0.01% |
| Western and Southern Coast of the GOM (WSC) | 153.81 | 147.01 | −6.80 | −4.4% | 1.19 | 0.77% | −1.90 | −1.29% |
| Total discharge to the GOM | 1101.54 | 1092.42 | −9.11 | −0.8% | 1.36 | 0.12% | −4.67 | −0.43% |

[a]The discharges from Lower Mississippi and Lower Missouri are the net discharge from these subbasins, i.e., total streamflow leaving from these basins minus streamflow from upper subbasins.

over wetland area, should be further calibrated against gauge observations. The model also needs further implementations on simulating land use influences such as dam constructions and irrigation projects. As to effects of land use and LC change on water fluxes, more and more watershed-level paired experiments and metadata analysis [e.g., *Bosch and Hewlett*, 1982; *Farley et al*., 2005; *Jackson et al*., 2005; *Sun et al*., 2005] have been conducted through recent decades, and these data sets could be used for further model evaluations and sensitivity analyses.

[53] Another limitation in this modeling study relates to meteorological data and simulation experiments on climate factors. In FixT and FixP experiments, $T$ and $P$ are fixed, respectively, but other factors such as humidity and solar radiations are transient. The reality is that all climate factors are always connected and influenced by each other. Therefore, the factor simulations might have big bias with realities. To improve the simulation experiments, a better solution would be to use regional climate models to generate high-resolution data set for driving this model or even

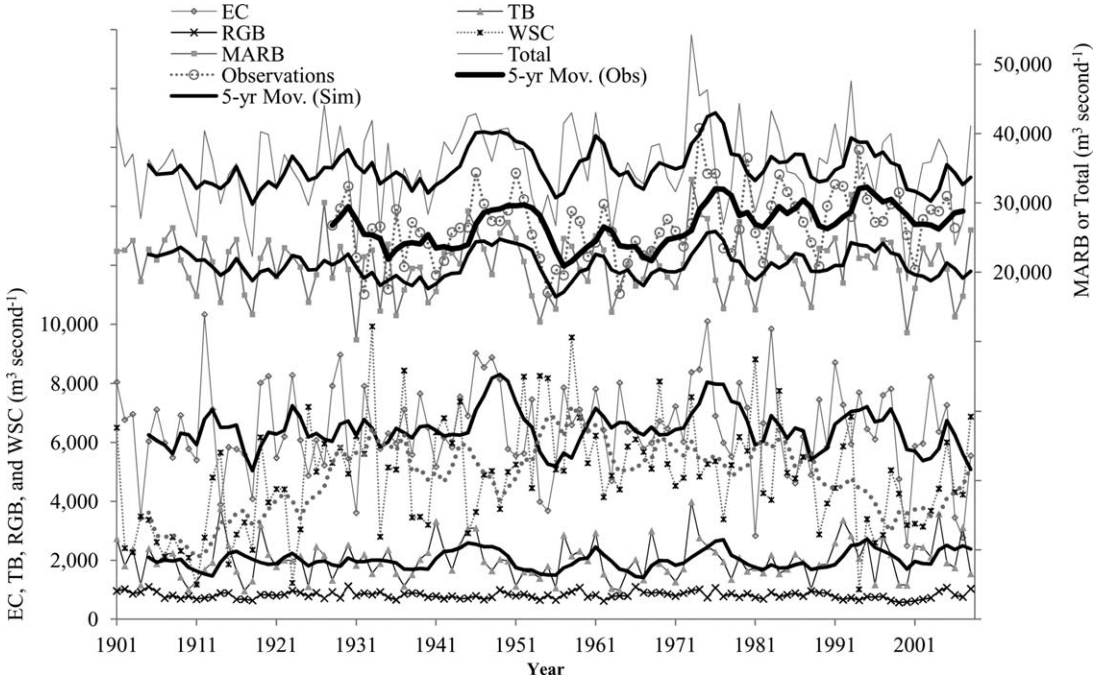


**Figure 12.** Estimated water discharges from each subbasin to the GOM during 1901–2008 and the total observed discharge from selected rivers) (unit: $m^3\ s^{-1}$). Note: The total GOM drainage area is larger than total drainage area of selected rivers (observations) by 25.7%.

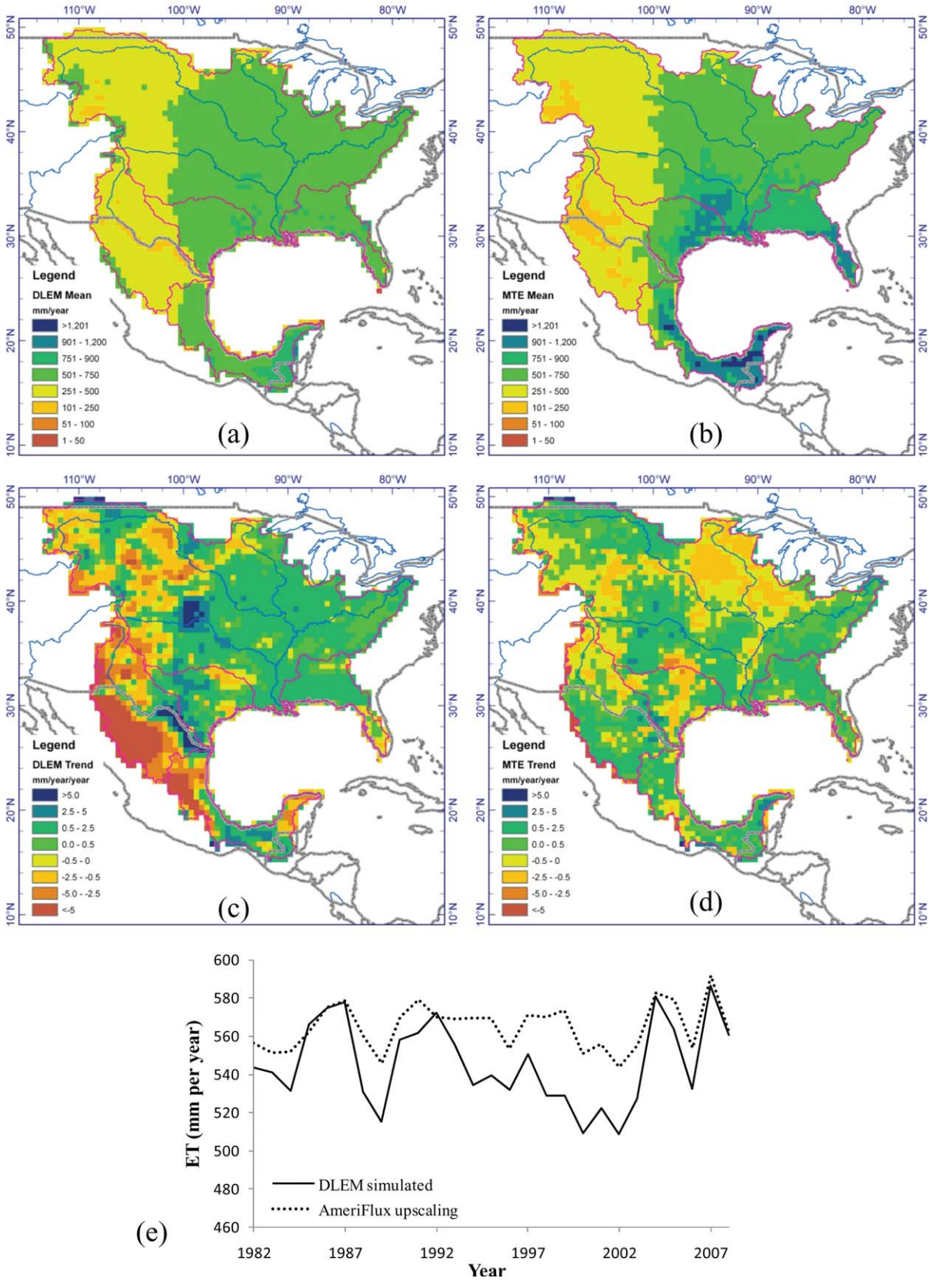


**Figure 13.** Simulated ET versus upscaled results by MTE (model tree ensemble) during 1982–2008. (a) DLEM simulated average annual ET; (b) MTE derived average annual ET; (c) linear trends in DLEM simulated annual ET (mm $yr^{-1}$ $yr^{-1}$); and (d) linear trends in MTE derived annual ET (mm $yr^{-1}$ $yr^{-1}$).

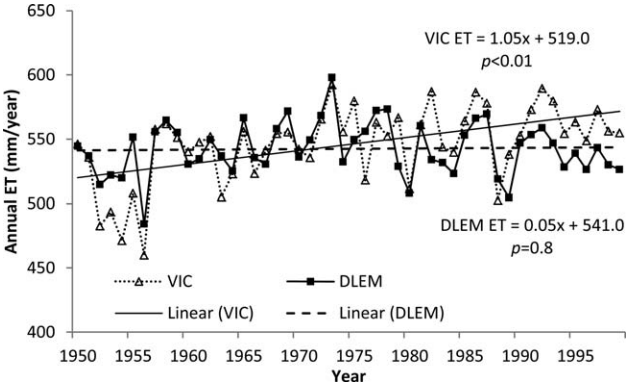


**Figure 14.** DLEM modeled ET versus VIC modeled ET [*Maurer et al*., 2002] over study area in the United States during 1950–1999.

further to couple DLEM with regional climate models to investigate the interaction and feedbacks between terrestrial ecosystems and land use with climate change.

## 7. Conclusions

[54] In this study, DLEM v2.0 was applied to investigate the spatial and temporal variations of ET, runoff, and runoff/precipitation ratio over the drainage basin of the GOM and to quantify interannual variations of total freshwater discharge to the ocean during 1901–2008. The agreement of simulated river discharge and ET with observations indicates that DLEM successfully captures the patterns of historical water fluxes from the scale of small watersheds to large river basins.

[55] In the past 108 years, the study area has been experiencing dramatic environmental changes in climate and land use. These environmental stresses were distributed unevenly across this large region. In conjunction with newly developed high-resolution spatial data, the improved DLEM has modified the cohort structure, explicit river routine, and rainfall subdaily disaggregation processes to reproduce historical water fluxes over the land and to quantify relative contributions from climate change and land use. Simulation results indicated a significant decreasing trend in ET at a rate of 15 mm $yr^{-1}$ $century^{-1}$ and a small increase in runoff during 1901–2008. The *R*/*P* ratio showed no significant long term trend over the study area. However, they all demonstrated substantial spatial heterogeneity across the study region and decadal fluctuations throughout the century-long period. Generally, in the west arid area and the southern area, ET, runoff, and *R*/*P* ratio all decreased during the last 108 years. Comparing to prior periods, the recent 30 years from 1979 to 2008 shows a conversion in *R* and total discharge from an upward trend to a downward trend, particularly in the EC, LOH, and WSC. ET also shows an increasing trend in all subbasins except in the RGB and WSC during 1979–2008.

[56] Factor simulation experiments results indicate that climate change was the dominant factor controlling the interannual variations of ET and runoff. More specifically, precipitation played the major role in shaping variations of annual water fluxes over the whole region. The effects of temperature on ET were generally moderated by the precipitation, particularly in water-limited area such as the west arid area of the GOM drainage basin. As to the long-term trends in water fluxes and R/*P* ratio, land use changes resulted in almost the same magnitude of impacts as climate change. Over the entire study region as a whole, both changes in land use and climate reduced ET during the last 108 years. However, their effects had significant spatial heterogeneity because of its uneven distributions in different microclimate conditions. Normally, urbanization decreased ET while reforestation and afforestation increased ET. The large reforestation area in the Appalachian Mountains significantly increased ET and decreased the *R*/*P* ratio during 1901–2008; while the deforestation processes in Mexico appears to have controversial effects. Modeled results did not find significant long-term trends in total freshwater discharge to the GOM in the past 108 years. However, the historical discharge showed substantial decadal fluctuations and differences among basins. During the recent 30 years, total freshwater discharge to the GOM has decreased by 12% compared to an increasing trend in prior period.

[57] To further investigate how climate change and human activities affect regional water resources, finer resolution of spatial data on water use and water projects including dam information should be considered in the modeling framework. In addition, uncertainties from the reconstructed meteorological data and the interactions between hydrological and biogeochemical processes should be further quantified in the future studies.

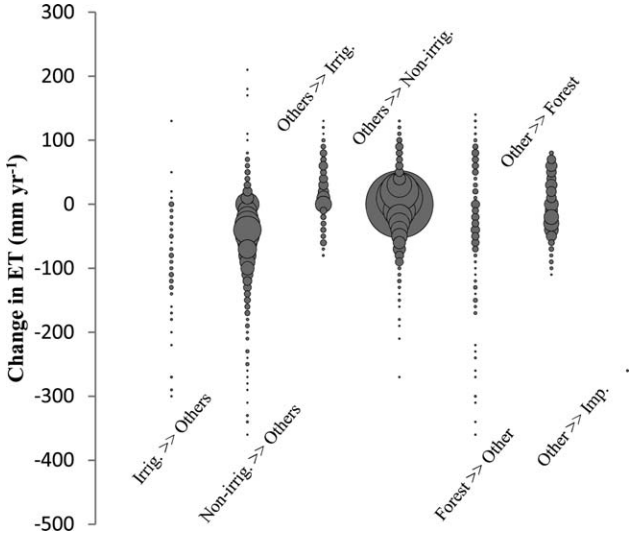


**Figure 15.** DLEM modeled change in ET due to land use and LC change. The circle area represents the relative accounts of grid cells fall in the change rate. Irriig. and Nonirrig. represent irrigated and nonirrigated cropland, respectively. "$>>$" represents conversion from one type to another type. The sampled grid cells for plotting this figure have more than 50% change in total area in each 5 arc min grid cell.

## Appendix A: Runoff Processes

[58] Surface runoff ($R_s$) (mm $H_2O$ $m^{-2}$ $s^{-1}$) is calculated as

$$R_s = t_{\text{rain}}\left(F'_{\text{sat}}\,Q_{\text{wat}} + \left(1 - F'_{\text{sat}}\right)\max\left(0, Q_{\text{wat}} - I_{\max}\right)\right) + (1 - t_{\text{rain}})\left(F'_{\text{sat}}\,Q_{\text{owat}} + \left(1 - F'_{\text{sat}}\right)\max\left(0, Q_{\text{owat}} - I_{\max}\right)\right), \tag{A1}$$

where $t_{\text{rain}}$ is the fractions of raining time; $F'_{\text{sat}}$ is the adjusted fractional saturated area ($F_{\text{sat}}$); $Q_{\text{wat}}$ is the total water input (including throughfall, snow melted water, and pond) (mm $H_2O$ $m^{-2}$ $s^{-1}$); $Q_{\text{owat}}$ is the total water input except for the throughfall (mm $H_2O$ $m^{-2}$ $s^{-1}$); $I_{\max}$ is the soil infiltration capacity depending on soil moisture and texture (mm $H_2O$ $m^{-2}$ $s^{-1}$) [*Entekhabi and Eagleson*, 1989; *Niu et al*., 2005]. Considering that wetland generally distributes in flat or slightly elevated areas in the landscape, it is assumed that 10% of estimated surface runoff leaves the wetland and the remaining is infiltrated into the soil column, i.e.,

$$R'_s = (1 - 0.9 f_{\text{wetland}})R_s, \tag{A2}$$

where $f_{\text{wetland}}$ is the fractional wetland within each grid cell.

[59] The adjusted fractional saturated area is calculated as

$$F'_{\text{sat}} = F_{\text{sat}} + (1 - F_{\text{sat}})f_{\text{imp}} \tag{A3}$$

where $F_{\text{sat}}$ is the fractional saturated area estimated with SIMTOP [*Niu et al*., 2005; *Niu and Yang*, 2006] and $f_{\text{imp}}$ is the fractional impervious surface area of each grid.

[60] Baseflow ($R_d$) (mm $H_2O$ $m^{-2}$ $s^{-1}$) is calculated as [*Oleson et al*., 2008]

$$R_d = \left(1 - f_{\text{imp,frz}}\right)R_{\text{d,max}}\, e^{(-f z_\nabla)} \tag{A4}$$

where $f_{\text{imp,frz}}$ is the fraction of impermeable area due to ice content of the soil layer interacting with water table [*Niu and Yang*, 2006]; $R_{d,\max} = 4.5\times10^{-4}$ mm $H_2O$ $m^{-2}$ $s^{-1}$ and $f = 2.5$ $m^{-1}$ [*Niu et al*., 2005]; $z^{\nabla}$ is the water table depth (m). Considering the fact of slow drainage from wetland, an adjustment for the grids that contain wetland is conducted in the same way as surface runoff (equation (A2)).

[61] The soil $T$ profile is formulated with the empirical method from *Katterer and Andren* [2009].

$$T_t(z) = T_{t-1}(z) + [T_{\text{surf}} - T_{t-1}(z)] \times e^{\left[-z\left(\frac{\pi}{k_s p}\right)^{1/2}\right]} \times \alpha \times e^{(-k_{\text{LB}}\,\text{LAI}_t)}, \tag{A5}$$

where $t$ is time (day); $z$ is soil depth (cm); $T_{\text{surf}}$ is the surface soil $T$ (°C), which is estimated as the 11 day moving average of air $T$ (°C); $k_s$ is the thermal diffusivity ($m^2$ $d^{-1}$); $p = 365$; LAI is leaf area index ($m^2$ $m^{-2}$) at $t$ day; $k_{\text{LB}}$ and $\alpha$ are attenuation factors and $k_{\text{LB}} = 0.15$ and $\alpha = 0.11$ is set from the calibration results of *Katterer and Andren* [2009].

## Appendix B: Evapotranspiration Processes

[62] The transpiration of the $j$th PFT from the $i$th soil layer is calculated as

$$(\text{trans}_i)_j = (\text{trans})_j \frac{(r_i)_j w_i}{\sum_{i=1}^{10}\left[(r_i)_j w_i\right]}, \tag{B1}$$

where $(r_i)_j$ is the $j$th PFT's root fractions in the $i$th layer, $w_i$ is the wetness of the $i$th soil layer, and $(\text{trans})_j$ (mm $H_2O$ $m^{-2}$ $s^{-1}$) is the total estimated transpiration of the $j$th PFT.

[63] The transpiration is calculated by the Penman-Monteith approach [*Wigmosta et al*., 1994]. The maximum transpiration is set as the root-weighted available soil water. In the Penman-Monteith equation, the canopy resistance is upscaled from the two-leaf model [*Campbell*, 1977; *Landsberg*, 1986]:

$$(g_c)_j = \frac{\text{LAI}_j^{\text{sun}}}{\left(r_s^{\text{sun}}\right)_j} + \frac{\text{LAI}_j^{\text{sha}}}{\left(r_s^{\text{sha}}\right)_j}, \tag{B2}$$

$$(r_c)_j = 1/(g_c)_j, \tag{B3}$$

where $g_c$ (m $s^{-1}$) and $r_c$ (s $m^{-1}$) is the canopy conductance and canopy resistance, respectively; $r_s^{\text{sun}}$ (s $m^{-1}$) and $r_s^{\text{sha}}$ (s $m^{-1}$) is the stomatal resistance of sunlit leaves and shaded leaves, respectively. The stomatal conductance is regulated by solar radiation, temperature, vapor pressure deficit, soil water potential, and atmospheric $CO_2$ concentration. The following equations are used to estimate the stomatal conductance, which is built upon a combination from *Jarvis and Morison* [1981], *Running and Coughlan* [1988], and *Chen et al*. [2005]:

$$g_s = \max\left(g_{\max} \times r_{\text{corr}} \times b \times f(\text{ppdf}) \times f(T_{\min}) \times f(\text{vpd}) \times f(\text{CO}_2),\ g_{\min}\right), \tag{B4}$$

where $r_{\text{corr}}$ is the correction factor of temperature and air pressure on conductance; $b$ is the factor of soil moisture; ppdf is the photosynthetic photo flux density (umol $m^{-2}$ $s^{-1}$); $T_{\min}$ is the daily minimum $T$ (°C); vpd is the vapor pressure deficit (pa); $CO_2$ is the atmospheric $CO_2$ concentration (ppm); $g_{\max}$ (m $s^{-1}$) and $g_{\min}$ (m $s^{-1}$) is the maximum and minimum stomatal conductance, respectively (m $s^{-1}$). The effect of each factor on stomatal conductance can be described as

$$r_{\text{corr}} = \left(\frac{T_{\text{day}} + 273.15}{293.15}\right)^{1.75} \times \left(\frac{101300}{\text{Pair}}\right), \tag{B5}$$

$$b_i = \begin{cases} 1 & \psi_i > \psi_{\text{open}} \\ \dfrac{\psi_{\text{open}} - \psi_i}{\psi_{\text{open}} - \psi_{\text{close}}}\psi_{\text{close}} \le \psi_i \le \psi_{\text{open}} & \\ 0 & \psi_i < \psi_{\text{close}} \end{cases}, \tag{B6}$$

$$b = \sum_{i=1}^{10}\left(\text{root}_i \times \frac{\theta_{\text{sat,i}} - \theta_{\text{ice,i}}}{\theta_{\text{sat,i}}} \times b_i\right), \tag{B7}$$

$$f(\text{ppdf}) = \frac{\text{ppdf}}{75 + \text{ppdf}}, \tag{B8}$$

$$f(T_{\min}) = \begin{cases} 1 & T_{\min} > 0^{\circ}C \\ 1 + 0.125T_{\min} & -8^{\circ}C \le T_{\min} \le 0^{\circ}C \\ 0 & T_{\min} < -8^{\circ}C \end{cases}, \tag{B9}$$

$$f(\text{vpd}) = \begin{cases} 1 & \text{vpd} < \text{vpd}_{\text{open}} \\ \dfrac{\text{vpd}_{\text{close}} - \text{vpd}}{\text{vpd}_{\text{close}} - \text{vpd}_{\text{open}}} & \text{vpd}_{\text{open}} \le \text{vpd} \le \text{vpd}_{\text{close}} \\ 0 & \text{vpd} > \text{vpd}_{\text{close}} \end{cases}, \tag{B10}$$

$$f(\text{CO}_2) = -0.001\text{CO}_2 + 1.35, \tag{B11}$$

where Pair is the air pressure (pa); $T_{\text{day}}$ is day time air temperature (°C); $\text{root}_i$ is the fractional root distribution in the $i$th soil layer [*Zeng*, 2001]; $\theta_{\text{sat},i}$ is the $i$th soil layer saturated volumetric water content ($\text{m}^3\ \text{m}^{-3}$); $\theta_{\text{ice},i}$ is the volumetric ice content of the $i$th soil layer; $\psi$ is the water potential (mm), which is controlled by the root-weighted soil moisture [*Oleson et al*., 2004]; $\psi_i$ (mm) is the water potential of the $i$th soil layer; $\psi_{\text{open}}$ (mm) and $\psi_{\text{close}}$ (mm) are the water potential under which the stomata fully open and close, respectively; $\text{vpd}_{\text{close}}$ (pa) and $\text{vpd}_{\text{open}}$ (pa) are the vapor pressure deficits (VPD) when the stomata fully close and open, respectively; the effect of atmospheric $CO_2$ on stomata conductance (i.e., $f(CO_2)$) is derived from the metadata analysis of *Ainsworth and Long* [2005].

[64] For the fraction of wetland and the irrigated cropland, the parameter $b$ is set as 1 (i.e., no soil moisture limitation on the transpiration).For irrigated cropland, if the estimated transpiration is larger than the available soil water, the water deficiency is assumed to be replenished with irrigation. For wetland, the estimated transpiration cannot be larger than the available soil water.

[65] In estimating soil evaporation, a revision of bare-ground evaporations from the FAO-56 is used [*Allen et al*., 1998]. Improvements are made to consider canopy effects on manipulating net radiation and aerodynamic resistance. First, the transferred shortwave radiation through canopy is used as the energy source in Penman-Monteith equation to estimate the potential soil evaporation (PSE). Then, the PSE is adjusted by the leaf area according to *Belmans et al*. [1983]:

$$\text{PSE} = \text{pet}_{\text{PM}} \times e^{-0.6\text{LAI}}, \tag{B12}$$

where $\text{pet}_{\text{PM}}$ ($\text{mm}\ H_2O\ \text{m}^{-2}\ \text{s}^{-1}$) is the potential ET estimated with Penman-Monteith method and LAI ($\text{m}^2\ \text{m}^{-2}$) is the average LAI over the land area.

## Appendix C: River Routing Process

[66] The river routing process simulates the dynamics of water storage on land surface and groundwater and transport of water through river networks across each grid cell. The water budget of the surface water pool ($W_s$) ($\text{m}^3$) and subsurface drainage pool ($W_d$) ($\text{m}^3$) can be described as

$$\frac{\text{d}(W_s)}{\text{d}t} = R_s - \frac{W_s}{t_s}, \tag{C1}$$

$$\frac{\text{d}(W_d)}{\text{d}t} = R_d - \frac{W_d}{t_d}, \tag{C2}$$

$$\frac{\text{d}(W_R)}{\text{d}t} = \left(\frac{W_s}{t_s} + \frac{W_d}{t_d}\right) \times (1 - A_w) + (P_w - E_w) \times A_w - \frac{W_R}{t_R} - F_{\text{irrig}} + F_{\text{in}}, \tag{C3}$$

where $t_s$ and $t_d$ is the residence time (s) of $W_s$ and $W_d$, respectively; $A_w$ is the fractional surface water area in each grid (including lake and stream); $W_R$ ($\text{m}^3$) is the surface water reservoirs (including water in lake and stream); $F_{\text{in}}$ is the total water flow from upstream cells ($\text{m}^3\ \text{s}^{-1}$); $F_{\text{irrig}}$ is the water withdrawal for irrigation ($\text{m}^3\ \text{s}^{-1}$); $P_w$ is the precipitation over the water surface ($\text{m}^3\ \text{s}^{-1}$); and $E_w$ is the evaporation from the water surface which is estimated with Priestly-Taylor equation ($\text{m}^3\ \text{s}^{-1}$). Here $t_s$ is set as 2 h as *Costa and Foley* [1997] and *Coe* [2000] did, and empirically set $t_d$ as 2 days. The allocation of water flow to lakes and streams is weighted by their surface area. The residence time of water in the river $t_{R,\text{riv}}$ is calculated as *Coe* [2000]:

$$t_{R,\text{riv}} = \frac{D}{u}, \tag{C4}$$

$$u = \min\left(u_{\max}, u_{\min}(i_c/i_0)^{0.5}\right), \tag{C5}$$

where $D$ is the distance between centers of the local and downstream grid (m); $u_{\max} = 5\ \text{m s}^{-1}$, which is the maximum river flow velocity [*Miller et al*., 1994]; $u_{\min}$ is the minimum river flow velocity, $u_{\min}$ is set as $0.8\ \text{m s}^{-1}$ [*Coe*, 2000]; $i_c$ is the downstream gradient ($\text{m m}^{-1}$); and $i_0$ is a reference gradient ($0.5\times10^{-4}\ \text{m m}^{-1}$). The residence time of water in the lake is assumed 10 times longer than the river [*Coe*, 2000].

## Appendix D: Reconstruction of Historical Meteorological Data

[67] The principle of combining of CRU and NARR is that the interannual variations of monthly $T$ and $P$ during 1901–1978 are consistent with CRU. The daily pattern comes from certain year of NARR data that randomly selected. The monthly maximum and minimum $T$ and $P$ in NARR that randomly selected from the historical period will be kept in the reconstructed data series. The daily reconstructed climate is estimated as

$$V'_{i,j,d} = V^{\text{NARR}}_{i',j,d} + d^{\text{NARR}}_{i',j,d} \times r'_{i,j}, \tag{D1}$$

where $V'_{i,j,d}$ is reconstructed met data in $i$ year, $j$ month, and $d$ day; $i'$ is randomly selected year of NARR data; $V^{\text{NARR}}_{i',j,d}$ is NARR daily met data; $r'_{i,j}$ is daily bias correction per deviation from the monthly maximum or minimum; $d^{\text{NARR}}_{i',j,d}$ is the daily deviation from the monthly maximum or minimum.

$$r'_{i,j} = \frac{D'_{i,j} \times \text{days}_j}{S^{\text{NARR}}_{i',j}}, \tag{D2}$$

$$D'_{i,j} = D^{\text{CRU}}_{i,j} - D^{\text{NARR}}_{i',j}, \tag{D3}$$

$$S^{\text{NARR}}_{i,j} = \sum_{d=1}^{\text{days}_j} d^{\text{NARR}}_{i,j,d}, \tag{D4}$$

$$d^{\text{NARR}}_{i,j,d} = \max\left(V\max^{\text{NARR}}_{i,j} - V^{\text{NARR}}_{i,j,d}, V^{\text{NARR}}_{i,j,d} - V\min^{\text{NARR}}_{i,j}\right), \tag{D5}$$

$$V\max^{\text{NARR}}_{i,j} = \max\left(V^{\text{NARR}}_{i,j,1}, V^{\text{NARR}}_{i,j,2} \ldots V^{\text{NARR}}_{i,j,days_j}\right), \tag{D6}$$

$$V\min^{\text{NARR}}_{i,j} = \min\left(V^{\text{NARR}}_{i,j,1}, V^{\text{NARR}}_{i,j,2} \ldots V^{\text{NARR}}_{i,j,days_j}\right), \tag{D7}$$

$$D^{\text{CRU}}_{i,j} = V^{\text{CRU}}_{i,j} - \overline{V}^{\text{CRU}}_{j}, \tag{D8}$$

$$D^{\text{NARR}}_{i,j} = V^{\text{NARR}}_{i,j} - \overline{V}^{\text{NARR}}_{j}, \tag{D9}$$

where $D^{\text{CRU}}_{i,j}$ and $D^{\text{NARR}}_{i,j}$ are the differences of monthly $T$ or $P$ between year $i$ and the average during 1981–2000 in CRU series and NARR series, respectively; $D'_{i,j}$ is total monthly bias of selected NARR data from NARR multiyear average in year $i$ and month $j$; and $S^{\text{NARR}}_{i,j}$ is the total deviation from the monthly maximum and minimum of $T$ or $P$.

[68] **Acknowledgments.** This study has been supported by NASA Interdisciplinary Science Program (NNX10AU06G), the U.S. Department of Energy (DOE) NICCR Program, and Auburn University Water Resources Center Integrated Watershed Project. We would like to thank Chaoqun Lu, Wei Ren, Chi Zhang, and Bo Tao for their help in collecting the data and calibrating the model. We thank Adam and Hamlet for their valuable discussion related to this paper, and Greg Gould and Julian Reyes for helping us edit the text. Thanks also go to Martin Jung (Max Planck Institute for Biogeochemistry) for providing the MTE data and Aiguo Dai for providing the reconstructed historical river discharge data. Eddy-flux tower sites are part of the AmeriFlux network, and we gratefully acknowledge the efforts of researchers at these sites. Sites are funded through grants from the DOE Office of Biological and Environmental Research (BER) unless otherwise noted. The flux level 4 data being used in this study were downloaded from the Carbon Dioxide Information Analysis Center (CDIAC) (ftp://cdiac.ornl.gov/pub/ameriflux/data/Level4/AllSites/).

## References

Ainsworth, E.A., and S.P. Long (2005), What have we learned from 15 years of free-air CO(2) enrichment (FACE)? A meta-analytic review of the responses of photosynthesis, canopy, *New Phytol.*, *165*(2), 351–371, doi:10.1111/j.1469-8137.2004.01224.x.

Allen, R.G., L.S. Pereira, D. Raes, and M. Smith (1998), *Crop evapotranspiration—Guidelines for computing crop water requirements, FAO Irrig. and Drainage Pap. 56, Food and Agric*. Organ. of the United Nations, Rome, Italy.

Andreassian, V. (2004), Waters and forests: From historical controversy to scientific debate, *J. Hydrol.*, *291*(1-2), 1–27, doi:10.1016/j.jhydrol.2003.12.015.

Baldocchi, D. et al. (2001), FLUXNET: A new tool to study the temporal and spatial variability of ecosystem-scale carbon dioxide, water vapor, and energy flux densities, *Bull. Am. Meteorol. Soc.*, *82*(11), 2415–2434, doi:10.1175/1520-0477(2001)082<2415:FANTTS>2.3.CO;2.

Batjes, N.H. (2006), ISRIC-WISE derived soil properties on a 5 by 5 arc-minutes global grid. (ver. 1.1). Report 2006/02, ISRIC - World Soil Information, Wageningen, http://www.isric.org/sites/default/files/isric_report_2012_01.pdf.

Belmans, C., J.G. Wesseling, and R.A. Feddes (1983), Simulation-model of the water-balance of a cropped soil—SWATRE, *J. Hydrol.*, *63*(3-4), 271–286, doi:10.1016/0022–1694(83)90045-8.

Bormann, H., L. Breuer, T. Graeff, and J.A. Huisman (2007), Analysing the effects of soil properties changes associated with land use changes on the simulated water balance: A comparison of three hydrological catchment models for scenario analysis, *Ecol. Modell.*, *209*(1), 29–40, doi:10.1016/j.ecolmodel.2007.07.004.

Bosch, J.M., and J.D. Hewlett (1982), A review of catchment experiments to determine the effect of vegetation changes on water yield and evapotranspiration, *J. Hydrol.*, *55*(1-4), 3–23, doi:10.1016/0022-1694(82)90117-2.

Cai, W. (2011), Estuarine and coastal ocean carbon paradox: CO(2) sinks or sites of terrestrial carbon incineration?, in *Annual Review of Marine Science*, vol. *3*, edited by C.A. Carlson and S.J. Giovannoni, pp. 123–145, Annual Reviews, Palo Alto, Calif.

Campbell, G.S. (1977), *An Introduction to Environmental Biophysics*, Springer, New York.

Chen, G., H. Tian, M. Liu, W. Ren, C. Zhang, and S. Pan (2006), *Climate impacts on China's terrestrial carbon cycle: An assessment with the dynamic land ecosystem model, in Environmental Modeling and Simulation*, edited by H. Tian, pp. 65–71, Acta Press, Anheim, Calif.

Chen, J., and P. Kumar (2001), Topographic influence on the seasonal and interannual variation of water and energy balance of basins in North America, *J. Clim.*, *14*(9), 1989–2014, doi:10.1175/1520-0442(2001)014<1989:TIOTSA>2.0.CO;2.

Chen, J., X. Chen, W. Ju, and X. Geng (2005), Distributed hydrological model for mapping evapotranspiration using remote sensing inputs, *J. Hydrol.*, *305*(1-4), 15–39, doi:10.1016/j.jhydrol.2004.08.029.

Coe, M.T. (2000), Modeling terrestrial hydrological systems at the continental scale: Testing the accuracy of an atmospheric GCM, *J. Clim.*, *13*(4), 686–704, doi:10.1175/1520-0442(2000)013<0686:MTHSAT>2.0.CO;2.

Connolly, R.D., J. Schirmer, and P.K. Dunn (1998), A daily rainfall disaggregation model, *Agric. For. Meteorol.*, *92*(2), 105–117, doi:10.1016/S0168-1923(98)00088-4.

Costa, M.H., and J.A. Foley (1997), Water balance of the Amazon Basin: Dependence on vegetation cover and canopy conductance, *J. Geophys. Res.*, *102*(D20), 23,973–23,989, doi:10.1029/97JD01865.

Dai, A., T. Qian, K.E. Trenberth, and J.D. Milliman (2009), Changes in continental freshwater discharge from 1948 to 2004, *J. Clim.*, *22*(10), 2773–2792, doi:10.1175/2008JCLI2592.1.

DeFries, R., and N. Eshleman (2004), Land-use change and hydrologic processes: A major focus for the future, *Hydrol. Process.*, *18*(11), 2183–2186, doi:10.1002/hyp.5584.

Dirmeyer, P., A. Dolman, and N. Sato (1999), The pilot phase of the Global Soil Wetness Project, *Bull. Am. Meteorol. Soc.*, *80*(5), 851–878, doi:10.1175/1520-0477(1999)080<0851:TPPOTG>2.0.CO;2.

Donner, S.D., M.T. Coe, J.D. Lenters, T.E. Twine, and J.A. Foley (2002), Modeling the impact of hydrological changes on nitrate transport in the Mississippi River Basin from 1955 to 1994, *Global Biogeochem. Cycles*, *16*(3), 16-1–16-9, doi:10.1029/2001GB001396.

Donner, S.D., C.J. Kucharik, and J.A. Foley (2004), Impact of changing land use practices on nitrate export by the Mississippi River, *Global Biogeochem. Cycles*, *18*, GB1028, doi:10.1029/2003GB002093.

Elvidge, C.D., B.T. Tuttle, P.S. Sutton, K.E. Baugh, A.T. Howard, C. Milesi, B.L. Bhaduri, and R. Nemani (2007), Global distribution and density of constructed impervious surfaces, *Sensors*, *7*(9), 1962–1979, doi:10.3390/s7091962.

Entekhabi, D., and P. S. Eagleson (1989), Land surface hydrology parameterization for atmospheric General Circulation models including subgrid scale spatial variability, *J. Clim.*, *2*(8), 816–831.

Environmental Protection Agency, Office of Water Gulf of Mexico Program (1994), Freshwater inflow action agenda for the Gulf of Mexico first generation-management committee report, EPA 800-B-94-006, U.S. Environ. Protect. Agency, Stennis Space Center, Miss.

Farley, K., E. Jobbagy, and R. Jackson (2005), Effects of afforestation on water yield: A global synthesis with implications for policy, *Global Change Biol.*, *11*(10), 1565–1576, doi:10.1111/j.1365–2486.2005.01011.x.

Fisher, J.B., K.P. Tu, and D.D. Baldocchi (2008), Global estimates of the land-atmosphere water flux based on monthly AVHRR and ISLSCP-II

data, validated at 16 FLUXNET sites, *Remote Sens. Environ.*, *112*(3), 901–919, doi:10.1016/j.rse.2007.06.025.

Foken, T. (2008), The energy balance closure problem: An overview, *Ecol. Appl.*, *18*(6), 1351–1367, doi:10.1890/06–0922.1.

Foley, J.A., C.J. Kucharik, T.E. Twine, M.T. Coe, and S.D. Donner (2004), Land use, land cover and climate change across the Mississippi basin: Impacts on selected land and water resources, in *Ecosystems and Land Use Change*, vol. *153*, edited by R. DeFries, G.P. Asner, and R.A. Houghton, pp. 249–261, AGU, Washington, D.C.

Foley, J. et al. (2005), Global consequences of land use, *Science*, *309*(5734), 570–574, doi:10.1126/science.1111772.

Food and Agriculture Organization of the United Nations (2006), *Fertilizer Use by Crop*, Food and Agric. Organ. of the United Nations, Rome.

Gedney, N., P. Cox, R. Betts, O. Boucher, C. Huntingford, and P. Stott (2006), Detection of a direct carbon dioxide effect in continental river runoff records, *Nature*, *439*(7078), 835–838, doi:10.1038/nature04504.

Goldewijk, K.K., and N. Ramankutty (2004), Land cover change over the last three centuries due to human activities: The availability of new global data sets, *Geojournal*, *61*, 335–344.

Graham, S.T., J.S. Famiglietti, and D.R. Maidment (1999), Five-minute,1/2 degrees, and 1 degrees data sets of continental watersheds and river networks for use in regional and global hydrologic and climate system modeling studies, *Water Resour. Res.*, *35*(2), 583–587, doi:10.1029/1998WR900068.

Guo, Z., P.A. Dirmeyer, Z.-Z. Hu, X. Gao, and M. Zhao (2006), Evaluation of the Second Global Soil Wetness Project soil moisture simulations: 2. Sensitivity to external meteorological forcing, *J. Geophys. Res.*, *111*, D22S02, doi:10.1029/2006JD007845.

Henderson-Sellers, B. (1984), A new formula for latent-heat of vaporization of water as a function of temperature, *Q.J. R. Meteorol. Soc.*, *110*(466), 1186–1190.

Huntington, T. (2006), Evidence for intensification of the global water cycle: Review and synthesis, *J. Hydrol.*, *319*(1-4), 83–95, doi:10.1016/j.jhydrol.2005.07.003.

Hutjes, R.W. A. et al. (1998), Biospheric aspects of the hydrological cycle, *J. Hydrol.*, *212*(1-4), 1–21, doi:10.1016/S0022-1694(98)00255-8.

Intergovernmental Panel on Climate Change (IPCC) (2007), *Climate Change 2007: The Physical Science Basis. Contribution of Working Group I to the Fourth Assessment Report of the Intergovernmental Panel on Climate Change*, edited by S. Solomon et al., p. 996, Cambridge Univ. Press, Cambridge, U.K.

Jackson, R., S. Carpenter, C. Dahm, D. McKnight, R. Naiman, S. Postel, and S. Running (2001), Water in a changing world, *Ecol. Appl.*, *11*(4), 1027–1045, doi:10.2307/3061010.

Jackson, R., E. Jobbagy, R. Avissar, S. Roy, D. Barrett, C. Cook, K. Farley, D. le Maitre, B. McCarl, and B. Murray (2005), Trading water for carbon with biological sequestration, *Science*, *310*(5756), 1944–1947, doi:10.1126/science.1119282.

Jarvis, P.G., and J.I. L. Morrison (1981), *The control of transpiration and photosynthesis by the stomata, in Stomatal Physiology*, edited by P.G. Jarvis and T.A. Mansfield, pp. 248–279, Cambridge Univ. Press, Cambridge.

Jung, M., M. Reichstein, and A. Bondeau (2009), Towards global empirical upscaling of FLUXNET eddy covariance observations: Validation of a model tree ensemble approach using a biosphere model, *Biogeosciences*, *6*(10), 2001–2013.

Jung, M., et al. (2010), Recent decline in the global land evapotranspiration trend due to limited moisture supply, *Nature*, *467*(7318), 951–954, doi:10.1038/nature09396.

Katterer, T., and O. Andren (2009), Predicting daily soil temperature profiles in arable soils in cold temperate regions from air temperature and leaf area index, *Acta Agric. Scand. B Soil Plant Sci.*, *59*(1), 77–86, doi:10.1080/09064710801920321.

Labat, D., Y. Godderis, J. Probst, and J. Guyot (2004), Evidence for global runoff increase related to climate warming, *Adv. Water Resour.*, *27*(6), 631–642, doi:10.1016/j.advwatres.2004.02.020.

Landsberg, J.J. (1986), *Physiological Ecology of Forest Production*, Academic, Sydney, Australia.

Latifovic, R., Z. Zhu, J. Cihlar, C. Giri, and I. Olthof (2004), Land cover mapping of north and central America—Global land cover 2000, *Remote Sens. Environ.*, *89*(1), 116–127, doi:10.1016/j.rse.2003.11.002.

Lawrence, D.M., P.E. Thornton, K.W. Oleson, and G.B. Bonan (2007), The partitioning of evapotranspiration into transpiration, soil evaporation, and canopy evaporation in a GCM: Impacts on land-atmosphere interaction, *J. Hydrometeorol.*, *8*(4), 862–880, doi:10.1175/JHM596.1.

Lehner, B., and P. Doll (2004), Development and validation of a global database of lakes, reservoirs and wetlands, *J. Hydrol.*, *296*(1-4), 1–22, doi:10.1016/j.jhydrol.2004.03.028.

Liu, M., and H. Tian (2010), China′s land cover and land use change from 1700 to 2005: Estimations from high-resolution satellite data and historical archives, *Global Biogeochem. Cycles*, *24*, doi:10.1029/2009GB003687.

Liu, M., H. Tian, G. Chen, W. Ren, C. Zhang, and J. Liu (2008), Effects of land-use and land-cover change on evapotranspiration and water yield in China during 1900–2000, *J. Am. Water Resour. Assoc.*, *44*(5), 1193–1207, doi:10.1111/j.1752-1688.2008.00243.x.

Liu, M., H. Tian, C. Lu, X. Xu, G. Chen, and W. Ren (2012), Effects of multiple environment stresses on evapotranspiration and runoff over eastern China, *J. Hydrol.*, doi:http://dx.doi.org/10.1016/j.jhydrol.2012.01.009.

MacCracken, M., et al. (2009), Vulnerability of semi-enclosed marine systems to environmental disturbances, in *Watersheds, Bays, and Bounded Seas: The Science and Management of Semi-Enclosed Marine Systems*, edited by E.R. Urban, Jr., et al., pp. 9–29, Island Press, Wash.

Maurer, E.P., A.W. Wood, J.C. Adam, D.P. Lettenmaier, and B. Nijssen (2002), A long-term hydrologically based dataset of land surface fluxes and states for the conterminous United States, *J. Clim.*, *15*(22), 3237–3251, doi:10.1175/1520-0442(2002)015<3237:ALTHBD>2.0.CO;2.

McLaughlin, S.B., S.D. Wullschleger, G. Sun, and M. Nosal (2007), Interactive effects of ozone and climate on water use, soil moisture content and streamflow in a southern Appalachian forest in the USA, *New Phytol.*, *174*(1), 125–136, doi:10.1111/j.1469–8137.2007.01970.x.

Mesinger, F., et al. (2006), North American regional reanalysis, *Bull. Am. Meteorol. Soc.*, *87*(3), 343–360, doi:10.1175/BAMS-87-3-343.

Miller, J.R., G.L. Russell, and G. Caliri (1994), Continental-scale river flow in climate models, *J. Clim.*, *7*(6), 914–928, doi:10.1175/1520-0442(1994)007<0914:CSRFIC>2.0.CO;2.

Milly, P.C. D., and K.A. Dunne (2001), Trends in evaporation and surface cooling in the Mississippi River basin, *Geophys. Res. Lett.*, *28*(7), 1219–1222, doi:10.1029/2000GL012321.

Mitchell, T.D., and P.D. Jones (2005), An improved method of constructing a database of monthly climate observations and associated high-resolution grids, *Int. J. Climatol.*, *25*(6), 693–712, doi:10.1002/joc.1181.

Monfreda, C., N. Ramankutty, and J.A. Foley (2008), Farming the planet: 2. Geographic distribution of crop areas, yields, physiological types, and net primary production in the year 2000, Global Biogeochem. Cycles, 22, GB1022, doi:10.1029/2007GB002947.

Mu, Q., F.A. Heinsch, M. Zhao, and S.W. Running (2007), Development of a global evapotranspiration algorithm based on MODIS and global meteorology data, *Remote Sens. Environ.*, *111*(4), 519–536, doi:10.1016/j.rse.2007.04.015.

Mu, Q., M. Zhao, and S.W. Running (2011), Improvements to a MODIS global terrestrial evapotranspiration algorithm, *Remote Sens. Environ.*, *115*(8), 1781–1800, doi:10.1016/j.rse.2011.02.019.

Mueller, B., et al. (2011), Evaluation of global observations-based evapotranspiration datasets and IPCC AR4 simulations, *Geophys. Res. Lett.*, *38*, L06402, doi:10.1029/2010GL046230.

Niu, G., and Z. Yang (2006), Effects of frozen soil on snowmelt runoff and soil water storage at a continental scale, *J. Hydrometeorol.*, *7*(5), 937–952, doi:10.1175/JHM538.1.

Niu, G., Z. Yang, R.E. Dickinson, and L.E. Gulden (2005), A simple TOPMODEL-based runoff parameterization (SIMTOP) for use in global climate models, *J. Geophys. Res.*, *110*, D21106, doi:10.1029/2005JD006111.

Niu, G.-Y., Z.-L. Yang, R.E. Dickinson, L.E. Gulden, and H. Su (2007), Development of a simple groundwater model for use in climate models and evaluation with gravity recovery and climate experiment data, *J. Geophys. Res.*, *112*, doi:10.1029/2006JD007522.

Oleson, K.W., and Y. Dai et al., (2004): Technical description of the Community Land Model (CLM), NCAR Technical Note NCAR/TN-461+STR, National Center for Atmospheric Research, Boulder, CO, 173 pp.

Oleson, K.W. et al. (2008), Improvements to the Community Land Model and their impact on the hydrological cycle, *J. Geophys. Res.*, *113*, G01021, doi:10.1029/2007JG000563.

Pan, M., A.K. Sahoo, T.J. Troy, R.K. Vinukollu, J. Sheffield, and E.F. Wood (2012), Multisource estimation of long-term terrestrial water budget for major global river basins, *J. Clim.*, *25*(9), 3191–3206, doi:10.1175/JCLI-D-11–00300.1.

Piao, S., P. Friedlingstein, P. Ciais, N. de Noblet-Ducoudre, D. Labat, and S. Zaehle (2007), Changes in climate and land use have a larger direct impact than rising $CO_2$ on global river runoff trends, *Proc. Natl. Acad. Sci. U.S. A.*, *104*(39), 15,242–15,247, doi:10.1073/pnas.0707213104.

Qian, T., A. Dai, and K.E. Trenberth (2007), Hydroclimatic trends in the Mississippi River basin from 1948 to 2004, *J. Clim.*, *20*(18), 4599–4614, doi:10.1175/JCLI4262.1.

Rabalais, N.N., R.E. Turner, and D. Scavia (2002a), Beyond science into policy: Gulf of Mexico hypoxia and the Mississippi River, *Bioscience*, *52*(2), 129–142, doi:10.1641/0006–3568(2002)052[0129:BSIPGO]2.0.CO;2.

Rabalais, N.N., R.E. Turner, and W.J. Wiseman (2002b), Gulf of Mexico hypoxia, A.K.A. "The dead zone," *Annual Review of Ecology and Systematics*, *33*, 235–263.

Ramankutty, N., and J.A. Foley (1999), Estimating historical changes in global land cover: Croplands from 1700 to 1992, *Global Biogeochem. Cycles*, *13*(4), 997–1027, doi:10.1029/1999GB900046.

Ren, W., H. Tian, M. Liu, C. Zhang, G. Chen, S. Pan, B. Felzer, and X. Xu (2007a), Effects of tropospheric ozone pollution on net primary productivity and carbon storage in terrestrial ecosystems of China, *J. Geophys. Res.*, *112*, D22S09, doi:10.1029/2007JD008521.

Ren, W., H. Tian, G. Chen, M. Liu, C. Zhang, A.H. Chappelka, and S. Pan (2007b), Influence of ozone pollution and climate variability on net primary productivit and carbon storage in China′s grassland ecosystems from 1961 to 2000, *Environ. Pollut.*, *149*(3), 327–335, doi:10.1016/j.envpol.2007.05.029.

Rotter, R.P., T.R. Carter, J.E. Olesen, and J.R. Porter (2011), Crop-climate models need an overhaul, *Nat. Clim. Change*, *1*(4), 175–177.

Running, S.W., and J.C. Coughlan (1988), A general-model of forest ecosystem processes for regional applications: 1. Hydrologic balance, canopy gas-exchange and primary production processes, *Ecol. Modell.*, *42*(2), 125–154, doi:10.1016/0304–3800(88)90112-3.

Schilling, K.E., K.-S. Chan, H. Liu, and Y.-K. Zhang (2010), Quantifying the effect of land use land cover change on increasing discharge in the Upper Mississippi River, *J. Hydrol.*, *387*(3-4), 343–345, doi:10.1016/j.jhydrol.2010.04.019.

Seitzinger, S.P., J.A. Harrison, E. Dumont, A.H. W. Beusen, and A.F. Bouwman (2005), Sources and delivery of carbon, nitrogen, and phosphorus to the coastal zone: An overview of global nutrient export from watersheds (NEWS) models and their application, *Global Biogeochem. Cycles*, *19*, GB4S01, doi:10.1029/2005GB002606.

Shi, X., J. Mao, P.E. Thornton, F.M. Hoffman, and W.M. Post (2011), The impact of climate, CO(2), nitrogen deposition and land use change on simulated contemporary global river flow, *Geophys. Res. Lett.*, *38*, L08704, doi:10.1029/2011GL046773.

Slack, J.R., A.M. Lumb, J.M. Landwehr, and Geoological Survey (U.S.) (1993), *Hydro-climatic Data Network (HCDN): Stream Flow Data Set, 1874–1988, U.S. Dep. of the Interior*, U.S. Geol. Surv., Denver, Colo.

Sun, G., S. McNulty, J. Lu, D. Amatya, Y. Liang, and R. Kolka (2005), Regional annual water yield from forest lands and its response to potential deforestation across the southeastern United States, *J. Hydrol.*, *308*(1-4), 258–268, doi:10.1016/j.jhydrol.2004.11.021.

Sun, G., et al. (2011), Upscaling key ecosystem functions across the conterminous United States by a water-centric ecosystem model, *J. Geophys. Res.*, *116*, G00J05, doi:10.1029/2010JG001573.

Thenkabail, P.S., et al. (2009), Global irrigated area map (GIAM), derived from remote sensing, for the end of the last millennium, *Int. J. Remote Sens.*, *30*(14), 3679–3733.

Thornton, P.E., and N.A. Rosenbloom (2005), Ecosystem model spin-up: Estimating steady state conditions in a coupled terrestrial carbon and nitrogen cycle model, *Ecol. Modell.*, *189*(1-2), 25–48, doi:10.1016/j.ecolmodel.2005.04.008.

Tian, H., G. Chen, M. Liu, C. Zhang, G. Sun, C. Lu, X. Xu, W. Ren, S. Pan, and A. Chappelka (2010a), Model estimates of net primary productivity, evapotranspiration, and water use efficiency in the terrestrial ecosystems of the southern United States during 1895–2007, *For. Ecol. Manage.*, *259*(7), 1311–1327, doi:10.1016/j.foreco.2009.10.009.

Tian, H., X. Xu, M. Liu, W. Ren, C. Zhang, G. Chen, and C. Lu (2010b), Spatial and temporal patterns of CH(4) and N(2)O fluxes in terrestrial ecosystems of North America during 1979–2008: Application of a global biogeochemistry model, *Biogeosciences*, *7*(9), 2673–2694, doi:10.5194/bg-7–2673-2010.

Tian, H., M. Liu, C. Zhang, W. Ren, X. Xu, G. Chen, C. Lu, and B. Tao (2010c), The dynamic land ecosystem model (DLEM) for simulating terrestrial processes and interactions in the context of multifactor global change, *Acta Geogr. Sin.*, *95*(9), 1027–1047.

Tian, H., et al. (2011a), China′s terrestrial carbon balance: Contributions from multiple global change factors, *Global Biogeochem. Cycles*, *25*, GB1007, doi:10.1029/2010GB003838.

Tian, H., X. Xu, C. Lu, M. Liu, W. Ren, G. Chen, J. Melillo, and J. Liu (2011b), Net exchanges of CO(2), CH(4), and N(2)O between China′s terrestrial ecosystems and the atmosphere and their contributions to global climate warming, *J. Geophys. Res.*, *116*, doi:10.1029/2010JG001393.

Turner, R.E., and N.N. Rabalais (2003), Linking landscape and water quality in the Mississippi river basin for 200 years, *Bioscience*, *53*(6), 563–572, doi:10.1641/0006–3568(2003)053[0563:LLAWQI]2.0.CO;2.

Vinukollu, R.K., E.F. Wood, C.R. Ferguson, and J.B. Fisher (2011a), Global estimates of evapotranspiration for climate studies using multi-sensor remote sensing data: Evaluation of three process-based approaches, *Remote Sens. Environ.*, *115*(3), 801–823, doi:10.1016/j.rse.2010.11.006.

Vinukollu, R.K., R. Meynadier, J. Sheffield, and E.F. Wood (2011b), Multi-model, multi-sensor estimates of global evapotranspiration: Climatology, uncertainties and trends, *Hydrol. Process.*, *25*(26, SI), 3993–4010, doi:10.1002/hyp.8393.

Vorosmarty, C., and D. Sahagian (2000), Anthropogenic disturbance of the terrestrial water cycle, *Bioscience*, *50*(9), 753–765, doi:10.1641/0006–3568(2000)050[0753:ADOTTW]2.0.CO;2.

Vorosmarty, C.J., B. Fekete, and B.A. Tucker (1998), River discharge database, version 1.1 (RivDIS v1.0 supplement). Data set. Available on-line [http://www.daac.ornl.gov] from Oak Ridge National Laboratory Distributed Active Archive Center, Oak Ridge, Tennessee, U.S.A. doi:10.3334/ORNLDAAC/199.

Wang, K., R.E. Dickinson, and S. Liang (2008), Observational evidence on the effects of clouds and aerosols on net ecosystem exchange and evapotranspiration, *Geophys. Res. Lett.*, *35*, L10401, doi:10.1029/2008GL034167.

Wang, K., R.E. Dickinson, M. Wild, and S. Liang (2010a), Evidence for decadal variation in global terrestrial evapotranspiration between 1982 and 2002: 1. Model development, *J. Geophys. Res.*, *115*, D20112, doi:10.1029/2009JD013671.

Wang, K., R.E. Dickinson, M. Wild, and S. Liang (2010b), Evidence for decadal variation in global terrestrial evapotranspiration between 1982 and 2002: 2. Results, *J. Geophys. Res.*, *115*, D20113, doi:10.1029/2010JD013847.

Wigmosta, M., L. Vail, and D. Lettenmaier (1994), A distributed hydrology-vegetation model for complex terrain, *Water Resour. Res.*, *30*(6), 1665–1679, doi:10.1029/94WR00436.

Xu, X., H. Tian, C. Zhang, M. Liu, W. Ren, G. Chen, C. Lu, and L. Bruhwiler (2010), Attribution of spatial and temporal variations in terrestrial methane flux over North America, *Biogeosciences*, *7*(11), 3637–3655, doi:10.5194/bg-7–3637-2010.

Zeng, X. (2001), Global vegetation root distribution for land modeling, *J. Hydrometeorol.*, *2*(5), 525–530, doi:10.1175/1525–7541(2001)002<0525:GVRDFL>2.0.CO;2.

Zhang, C., H. Tian, A.H. Chappelka, W. Ren, H. Chen, S. Pan, M. Liu, D.M. Styers, G. Chen, and Y. Wang (2007a), Impacts of climatic and atmospheric changes on carbon dynamics in the Great Smoky Mountains National Park, *Environ. Pollut.*, *149*(3), 336–347, doi:10.1016/j.envpol.2007.05.028.

Zhang, K., J.S. Kimball, R.R. Nemani, and S.W. Running (2010), A continuous satellite-derived global record of land surface evapotranspiration from 1983 to 2006, *Water Resour. Res.*, *46*, W09522, doi:10.1029/2009WR008800.

Zhang, X., F.W. Zwiers, G.C. Hegerl, F.H. Lambert, N.P. Gillett, S. Solomon, P.A. Stott, and T. Nozawa (2007b), Detection of human influence on twentieth-century precipitation trends, *Nature*, *448*(7152), 461–465, doi:10.1038/nature06025.

Zhang, Y., and K. Schilling (2006), Effects of land cover on water table, soil moisture, evapotranspiration, and groundwater recharge: A field observation and analysis, *J. Hydrol.*, *319*(1-4), 328–338, doi:10.1016/j.jhydrol.2005.06.044.

Zhang, Y., F.H. S. Chiew, L. Zhang, and H. Li (2009), Use of remotely sensed actual evapotranspiration to improve rainfall-runoff modeling in Southeast Australia, *J. Hydrometeorol.*, *10*(4), 969–980, doi:10.1175/2009JHM1061.1.